Feedback control of a piezo deformable mirror for a wavefront-sensorless AO setup

Hendrik Kroese

Master of Science Thesis

Delft University of Technology

Delft Center for Systems and Control

Feedback control of a piezo deformable mirror for a wavefront-sensorless AO setup

Master of Science Thesis

For the degree of Master of Science in Systems and Control at Delft University of Technology

Hendrik Kroese

December 18, 2009

Faculty of Mechanical, Maritime and Materials Engineering · Delft University of Technology

Delft University of Technology
Department of
Delft Center for Systems and Control (dcsc)

The undersigned hereby certify that they have read and recommend to the Faculty of Mechanical, Maritime and Materials Engineering for acceptance a thesis entitled

Feedback control of a piezo deformable mirror for a wavefront-sensorless AO setup

by

Hendrik Kroese

in partial fulfillment of the requirements for the degree of

Master of Science.

Dated: December 18, 2009

Supervisor: ______________________
Prof.dr.ir. M.H.G. Verhaegen

Readers: ______________________
Msc. H. Song

____
dr.ir. G. Schitter

____
dr.ir. G. Vdovin

Abstract

This report describes the research on a wavefront-sensorless (WFSless) adaptive optics (AO) setup, where light intensity of a focussed beam behind a pinhole is measured. As wavefront compensator, a Piezo Deformable Mirror (PDM) was used. The goal of the research is to investigate which algorithms lead to the highest light intensity possible and the time needed to reach this optimum. The research consists out of two parts: compensation for the hysteresis of the PDM, which now causes inaccuracy of the actuator strokes; and implementation of theories on WFSless AO found in literature.

To reduce the effects of hysteresis, compensation was developed, which uses a modified structure of the Coleman-Hodgdon equations (C-H eq.). The inverse model can directly be used and the number of variables was reduced.

The optimization algorithms used to find light intensity are a Nelder-Mead (NM) simplex which directly optimizes PDM actuator voltages (VO), a NM, which controls 14 Zernike modes and a line search (LS) and quadratic optimization (QO) algorithm that optimize 14 individual Zernike modes coefficients. The OA and the hysteresis compensator were experimentally evaluated.

From the experimental tests it can be concluded that the NM algorithms result in the highest light intensity. The use of Zernike modes increases the optimization speed. For the NM simplex a reduction of 59-66% in time was achieved before the algorithm reached 95% of its final light intensity value. If the NM simplex in Zernike mode optimization is compared with the QO, the QO only needs 60 steps to reach a photodiode value of 3V (about 80% of highest possible light intensity), whereas the NM simplex needs 129 steps. The use of hysteresis compensation led to an increase of the light intensity for the NM in VO and the LS and QO.

Preface

This document is the result of my graduation project, done at the Faculty of Mechanical, Maritime and Materials Engineering at the Technical University of Delft. The project is the final work before receiving the title of Master of Science in Mechanical Engineering.

From my childhood I was fascinated by watching the stars. Even now I can stop in the middle of the fields and look up after a day of Delft and be amazed by its beauty. This led me to work on this adaptive optics project.

I would like to thank Hong Song and Michel Verhaegen for their support and advice during the project, Flexible Optical for providing the mirror and their advise for modeling it, Arjan van Dijke for his endless support to get the dSpace system working (again), Kees Slinkman for his help with electronics, Jan-Willem van Wingerden en Ivo Houtzager for their advice on embedded coding and Kitty Dukker for her help with al my administrative problems. Also I want to thank the colleagues that became my friends during my study in Delft for their fruitful discussions and advice, especially Karin Hoetmer and Sebastiaan Zaaijer. At last I want to thank my parents and my girlfriend Elena for their unconditional support.

Delft, December 18, 2009

Hendrik Kroese

Table of Contents

List of Figures

List of Tables

"The most precious things in life are not those one gets for money."
— *Albert Einstein*

Chapter 1

Introduction

Optical systems are limited in resolution, due to disturbances. It is possible to eliminate or reduce these disturbances by altering optical properties, resulting in a higher resolution. The field of Adaptive Optics (AO) deals with altering optical properties. This field is used in e.g. astronomy, medical issues, data transmission and laser beam shaping.

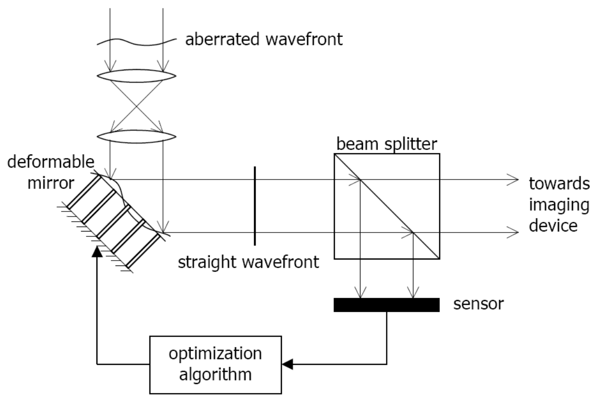

Figure 1-1: Schematics of an adaptive optics setup.

The principle of AO is shown in Figure 1-1. The aberration present in the incoming light is compensated by a wavefront compensator, in this case a deformable mirror (DM). The voltages that drive the DM are calculated by an optimization algorithm (OA), which receives information from a sensor. The beam splitter diverges part of the light to the sensor, the rest of the light will go to an imaging device.

In this thesis a Piezo Deformable Mirror (PDM) is used, because of its fast response and its ability to produce large amplitude wavefront manipulations, which is required in many applications. However hysteresis limits the accuracy of the PDM. Therefore this thesis will also investigate methods to reduce the influence of hysteresis.

Different sensor types exist. A commonly used sensor is the Shack-Hartmann wavefront sensor (WFS), which reconstructs the wavefront, by measuring local gradients. But the use of a camera in the WFS adds to the complexity of the AO system, especially in the case of real-time control. In some applications the use of WFSs is even impossible and only intensity measurement is possible.

This thesis investigates an alternative, using a photodiode to maximize the light intensity behind a pinhole. If the pinhole has the correct size and is placed at the correct location, then the photodiode will measure maximum light intensity in case all aberrations are compensated. This method of wavefront-sensorless (WFSless) sensing, where the wavefront is not reconstructed, is simple in hardware, since it does not require many components. This also reduces the cost of the sensor, compared to WFSs. Downside is that only the intensity is measured and there is no direct information about the shape of the wavefront. The OA should be able find the optimum with this limited information.
In the past, research was conducted that used the light intensity measured by photodiode for wavefront compensation. However in recent WFSless AO research, the focus is on the use of cameras. In the few cases light intensity is optimized, it is in a simulation. This thesis used the new insights in WFSless AO to maximize the light intensity after a pinhole.

Goal of this thesis is to maximize the light intensity measured by the photodiode of the experimental setup by controlling the voltage of the PDM. While doing this, two problems need to be taken into account: limited sensor information and non-linearity due to hysteresis of the piezo electric actuators of the DM. Limited sensor information implies that the OA has to be able to find the best compensation, without knowing on forehand which mirror shape it needs to produce. Hysteresis needs to be compensated, since it can reduce the convergence speed of the algorithm. By compensating hysteresis, uncertainty of the cost functions can be reduced.

First step of the research was to extract hysteresis, present in the PDM, with the Foucault knife edge test. Based on the Coleman-Hodgdon equations (C-H eq.), a hysteresis compensator was developed for the found hysteresis curves. Maximizing the intensity behind the pinhole was experimentally tested with the help of OAs. Voltage optimization (VO) was performed with the Nelder-Mead (NM) simplex. The NM simplex was also tested in shape optimization (SO) with Zernike modes. SO was also tested by applying a line search method and a quadratic optimization (QO). The OAs and hysteresis compensator were experimentally evaluated.

Now let us move on to the structure of the report. In Chapter 2 the basic principles of wavefront-sensorless adaptive optics are explained, the setup is introduced and the performance criteria are discussed. The properties of the PDM and the optical pathway are introduced in Chapter 3. A method for compensation of hysteresis of the mirror is presented in Chapter 4. Possible control algorithms to maximize the intensity after the pinhole are described in Chapter 5. In Chapter 6, the results of implementation of the algorithms and the use of hysteresis compensation are discussed. The conclusions of the present research and some recommendations on further studies are presented in Chapter 7.

Chapter 2

Problem Discussion

2-1 Adaptive optics in a nut-shell

All processes that do observations suffer from distortions, sometimes due to internal processes, sometimes due to external influences. The world of optics is not different. Optical distortions can sincerely reduce the resolution of image compared to ideal circumstances. However, just like the other fields, it is sometimes possible to minimize the influence of these aberrations. Adaptive optics (AO) is a technology used to improve the performance of optical systems by reducing the effects of optical distortion. In AO light is changed to fulfill the desired properties [1][2]. In case of observations like in astronomy or microscopy, aberrations are most times corrected with a deformable mirror (DM); a mirror with a thin surface, of which the shape is formed by actuators. The shape of aberrations produced by correction devices is called wavefront (Chapter 3-2). The desired wavefront shape is totally flat and is called ϕ_0. AO setups can be schematically depicted like the block diagram in Figure 2-1. Distorted light with wavefront ϕ_{ab}, is corrected by a DM, which produces ϕ_{dm}. The error in the wavefront ϕ_{error} left produces a sensor signal.

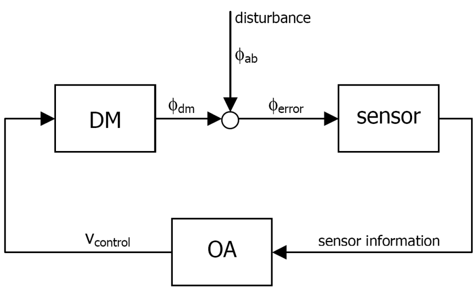

Figure 2-1: Block diagram of an adaptive optics setup.

The sensors can be divided into two categories: direct sensing and indirect sensing. With direct sensing the wavefront is immediately reconstructed; it is directly known which shape the wavefront compensator has to take in order to compensate for the aberrations. Indirect sensing does not reconstruct the wavefront pattern. Sometimes this method of sensing is called wavefront-sensorless, since the sensor does not reconstruct the wavefront. This method is till now mostly used in industrial and medical applications [3]. In the upcoming two Subsections the principles behind the two methods are explained.

2-1-1 Wavefront sensor AO

AO systems with wavefront sensors (WFS) identify the shape of the aberration after the wavefront compensator. This can be done in multiple ways. A commonly used sensor is the Shack-Hartmann sensor. This sensor consists of an array of lenses in front of a camera. In case of a flat wavefront, these lenses have their focal point at a certain place on the camera image. The disturbed wavefront causes the spot to move. By measuring the displacement of the spots in x and y direction, the average gradients of the wavefront at the location of those lenses are known (since the focal length is also known). From the gradients the wavefront pattern can be derived. If the shape of

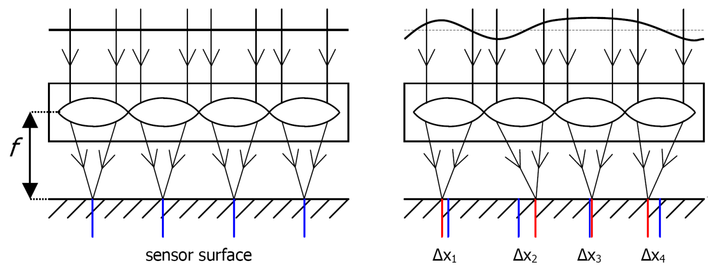

Figure 2-2: Principle of the Shack-Hartmann wavefront sensor: Aberrated light causes displacements of the focal points. The displacements can be converted into gradients, which are used to reconstruct the wavefront.

aberration left in the system is known, then the negative shape of this aberration should be added to the shape of the mirror to compensate for for this left-over aberration. As result, a flat wavefront will emerge after the DM.

2-1-2 Wavefront-sensorless AO

In wavefront-sensorless (WFSless) AO the shape of the wavefront is not reconstructed. This directly leads to the fact that it is impossible to directly know which shape the mirror has to take in order to compensate for aberrations still left in the AO setup. Most WFSless setups use a lens to focus the light beam in a plane, however the components for further analysis differ. Sometimes a camera is used to analyze the light pattern. This thesis handles the case where the light is focussed on a pinhole. Part of the light falls through the pinhole and is collected by the photodiode. In case of no aberration present, all light falls through the pinhole and maximum intensity is measured. In case of aberration an optimization algorithm (OA) is used to maximize the light intensity.

The lens/pinhole/photodiode intensity test consists of a pinhole that is placed at the focal point of a light beam without aberration that passes through a lens. A photodiode is placed behind the pinhole. The photodiode measures the light intensity. If the light beam does not have aberration, all the light will pass through the pinhole and the diode will measure maximum intensity. If the wavefront is aberrated, part of the light will not pass through the pinhole and the intensity will be lower. This is depicted in figure 2-3. When the intensity is at the global maximum, the wavefront is likely to have the least possible amount of aberration (and the picture is sharp as possible). However this implies that less information is available about the aberration, since the optimization algorithm does not directly known which voltages it has to apply to the mirror in order to obtain the highest light intensity.

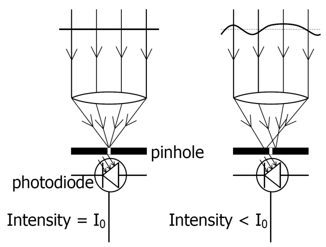

Figure 2-3: Principle of WFSless AO control where light intensity is used as control signal. Left: flat wavefront leading to maximum intensity I_0. Right: aberrated wavefront leading to a lower intensity, since part of the light is blocked by the pinhole surface.

The advantage of this sensor type is it limited amount of components, which simplifies the setup and keeps the costs low. Because the photodiode produces only a single voltage signal, which can in the future easily be connected to a programmable chip, creating a cheap controller. Cameras on the contrary require use of a pc to analyze images, which increases the size and costs of the control hardware. The lens/pinhole/photodiode method is chosen as sensor for the AO setup, because of its low costs, simplicity in hardware and its ability to be used in situations where the use of cameras is not possible.

2-2 Experimental setup

Figure 2-4 shows schematic presentation of the setup. In the next Subsections the system and its components will be explained in more detail.

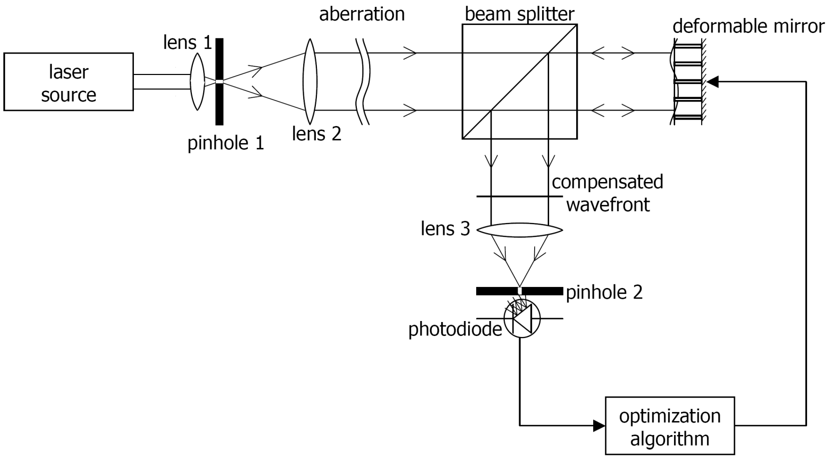

Figure 2-4: Schematics of the used WFSless AO experimental setup, where light intensity after the pinhole is maximized.

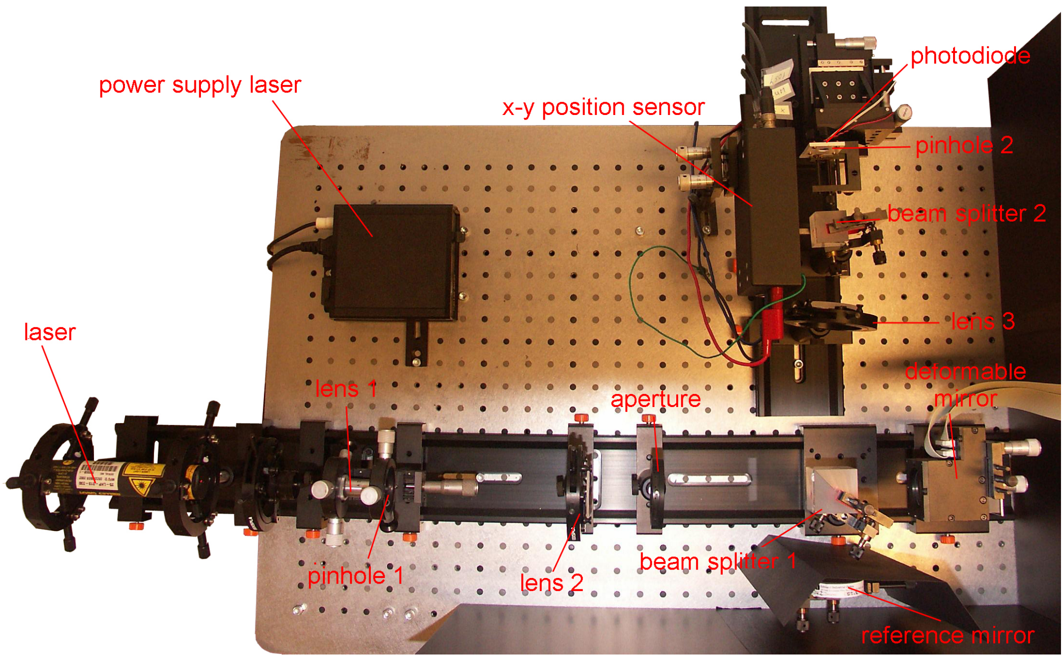

Figure 2-5: Photo of the used WFSless AO experimental setup.

2-2-1 Configuration of components

A laser beam is used as a light source. The beam is focussed with the help of lens 1 onto pinhole 1. After the pinhole the light can be regarded as a point source without aberration. Lens 2 converts the divergent light beam into a coherent light beam. If a piece of glass is used as disturbance, the aberration is introduced before the beam splitter. The beam continues its path, going through the beam splitter towards the piezo deformable mirror. The mirror adds a wavefront ϕ_{dm} to the aberrated wavefront. The reflected light on the mirror travels back through the beam splitter where a part goes straight and a part goes to lens 3, which focusses the light. If the beam is corrected properly, all focussed light will travel through pinhole 2 and the photodiode will measure maximum intensity. If the light beam is not focussed on the pinhole, part of the light will not go through the pinhole and the measured intensity will be less.

2-2-2 Aberration

The aberration in the setup was static. These aberrations were introduced in multiple ways. One aberration, that is always present in the system, is misalignment of optical components. Lenses which are not placed at the exact right position can cause defocus. This can also happen if the pinhole is shifted in z direction. If the pinhole is shifted in x or y direction, tip and tilt are introduced in the AO system. Another source of aberration can be the placement of a piece of glass in the optical pathway, however this was not experimentally tested. Last origin of aberration was by applying offsets voltages to the mirror. This type of aberration can be easily altered, to simulate different aberrations.

2-2-3 Pinhole

The formula of the intensity I after the pinhole is [4]:

$$I_{pinhole} = \int\int_{pinhole} |\mathcal{F}\{A(u,v)\}|^2 \, \mathrm{d}u\mathrm{d}v \tag{2-1}$$

with

$$A(\xi,\eta) = A_0(\xi,\eta) \cdot e^{i(\phi_{ab}(\xi,\eta)+\phi_{dm}(\xi,\eta)+\phi_{lens}(\xi,\eta))}. \tag{2-2}$$

The coordinates in the light beam are described by ξ and η. u and v are the coordinates that describe the surface of the pinhole. The photodiode has only one output signal: the light intensity. From this signal the wavefront error can not directly be reconstructed. Thus the choice of the lens/pinhole/photodiode combination results in limited sensor information; the only thing known, is that a higher light intensity means better compensation. The algorithm has to find which way it needs to deform the mirror, in order to get the highest light intensity (and thus have the flattest wavefront after compensation).

2-2-4 Piezo deformable mirror

The PDM has 37 actuators which are placed according to Figure 3-1. The surface shape is determined by the elongation of the actuators, which is again dependent on the applied voltage. Therefore, the wavefront that the mirror produces depends on the control voltages.

$$\phi_{dm} = f(V_{control}) \tag{2-3}$$

The corrected wavefront after the PDM is:

$$\phi_{error} = \phi_{ab} + \phi_{dm} \tag{2-4}$$

In case of perfect compensation, $\phi_{error}(\xi, \eta) = 0$, this implies $-\phi_{dm}(\xi, \eta) = \phi_{ab}(\xi, \eta)$; the wavefront of the DM has taken the negative form of the aberration.

A big downside of piezo actuators is that they suffer from hysteresis. The voltage applied to the actuator at a certain time instance is not enough to know the displacement of the actuator (and the corresponding surface profile). The history of the applied voltages is also of importance. The presence of hysteresis can degrade the performance of the optimization algorithm, causing the optimum to be found slower, or even result in a lower light intensity after optimization. More information about hysteresis and how it can be compensated, can be found in Chapter 4.

2-2-5 Control system

The OA was programmed in a Simulink-model, which was converted to c-code and uploaded to a dSpace-system. This implies that some of the built-in functions in Matlab could not be used, and needed to be programmed by the user. Big advantage of the dSpace system is that it approximates the ultimate goal of WFSless AO where the lens/pinhole/photodiode combination as sensor is used. It is not possible to implement a camera in the dSpace system. Also, if the optimization works on dSpace, it will be a relatively small step to replace the dSpace system by a chip.

2-3 Problem formulation

In order to remove the effects of aberrations the optimization algorithm maximizes the light intensity after a pinhole. The algorithm knows that the highest light intensity corresponds with an as flat as possible wavefront, but the photodiode signal itself does not give any information what shape the PDM has to take. The goal of this thesis is to compensate for a static wavefront aberration as much as possible with a piezo deformable mirror as wavefront compensator and the lens/pinhole/photodiode combination as sensor . Objective is to find the best voltage combination $V^*_{control}$ for the DM, so that wavefront aberration is minimized. This minimization is done by maximizing the intensity of the photodiode. The intensity depends on the shape of the aberration and the shape of the mirror, which on its turn depends on the control voltages. By combining equations 2-1 and 2-3, the objective can be defined.

$$V^*_{control} = \arg \max_{V_{control}} I(V_{control}, \phi_{ab}) \tag{2-5}$$

Aberration ϕ_{ab} is not known and the intensity is non-linear with respect to the voltages. As is visible in equation 2-1, it is not possible to find the shape of the aberration directly if the intensity is measured. This implies that an optimization algorithm is needed to find the optimal shape of the mirror. The optimization algorithm must be able to solve a multidimensional problem, since the surface shape is formed by 37 actuators. The optimization algorithm should also be able to handle non-linearities, since equation 2-1 is non-linear. Since hysteresis can decrease the convergence speed of the algorithm or even change the convexity of the cost function, it is wise to compensate for the hysteresis. This can be done by linearizing the PDM.

2-4 Performance criteria

This research investigates methods to optimize the light intensity after the pinhole of the setup shown in Figure 2-4. Starting point is the Nelder-Mead (NM) simplex where actuator voltages are directly optimized. This optimization algorithm proved to be successful in the past in combination with a micro-machined deformable mirror [5] and a thermal deformable mirror [4].

The criteria is as follows: the new optimization algorithms need to converge quicker than the standard situation using voltage based NM optimization, while still achieving the same or an even higher light intensity after the pinhole. A possible method for speeding up the optimization is the addition of a hysteresis compensator, with the voltage based NM OA, or with other OAs.

Chapter 3

Plant Model

This Chapter provides a more detailed background of the components in the experimental setup. In Section 3-1 the properties of the PDM are given and the relationship between driving voltages and mirror shape is described. Section 3-2 gives notations to describe the wavefront. In Section 3-3 the pinhole size is calculated and a formula of the light intensity is provided. In the last Section the properties of the high voltage amplifier are listed.

3-1 Properties of the piezo deformable mirror

3-1-1 General properties

The PDM is produced at Flexible Optical B.V. (OKO® Technologies) in Delft. The mirror has 37 piezoelectric column actuators that push and pull the mirror surface. The actuators are placed in hexagonal grid, as can be seen in Figure 3-1.
The maximum stroke that can be produced is 8μm at 400V. The mirror has a diameter of 30 mm. Other useful PDM properties are listed in Table 3-1 [6].

3-1-2 Hysteresis

As mentioned in Chapter 2-2-4 PDM actuators suffer from hysteresis. As a consequence, there is no linear relationship between input voltages and the mirror surface shape. The force and elongation, produced by the actuators, is also dependent on the history of the input voltage. Possible compensation methods for this behavior will be given in Chapter 4.

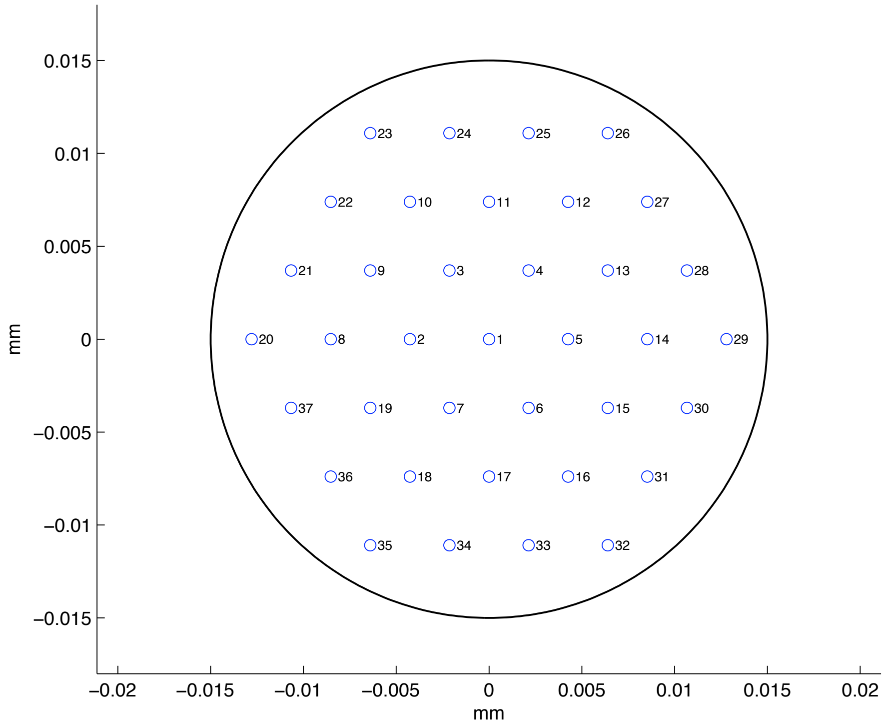

Figure 3-1: Placement of the actuators of the piezo deformable mirror.

3-1-3 Deformation of mirror surface

The surface of the PDM can be described with the help of the "thin plate model" [4][6]. According to this model, the surface can be described with a n number of points at location $\boldsymbol{z}$, with $\boldsymbol{z} \in \mathbb{R}^n$. $\boldsymbol{z}$ describes the location of observation points in the complex plane with $\boldsymbol{z} = \boldsymbol{r}\cos(\boldsymbol{\phi}) + i\boldsymbol{r}\sin(\boldsymbol{\phi})$. The plate is deformed by k actuators at location $\boldsymbol{\zeta}$, with $\boldsymbol{\zeta} \in \mathbb{R}^k$. $\boldsymbol{\zeta} = \boldsymbol{\rho}\cos(\boldsymbol{\psi}) + i\boldsymbol{\rho}\sin(\boldsymbol{\psi})$. Height $h(z)$ at location z can be described with the biharmonic equation [4]:

$$\nabla^4 h(z) = \frac{P(\zeta)}{D_k} \tag{3-1}$$

with P point like forces produced by the actuators and D_k the cylindrical rigidity [7]:

$$D_k = \frac{E \cdot h_k^3}{12 \cdot (1 - \nu^2)} \tag{3-2}$$

with E the Young modulus, h_k the thickness of the mirror plate and ν the Poison ratio of the of the reflective plate.
Laplacian operator ∇^2 for cylindrical coordinates is as follows:

$$\nabla^2(z) = \nabla^2(r, \phi) = \frac{\partial^2}{\partial r^2} + \frac{1}{r}\frac{\partial}{\partial r} + \frac{1}{r^2}\frac{\partial^2}{r^2 \partial \phi^2} \tag{3-3}$$

The solution for biharmonic equation 3-1 in case of mirror free, unsupported edges is:

$$h(z) = \frac{P}{16\pi D} W(z, \zeta) + W_0 + W_1 r\cos(\phi) + W_2 r\sin(\phi) \tag{3-4}$$

Table 3-1: Parameters of the PDM

Quantity	Value	Unit
Actuators		
Maximum voltage	400	[V]
Maximum stroke	$8 \cdot 10^{-6}$	[m]
Actuator pitch	$4.3 \cdot 10^{-3}$	[m]
Actuator pitch	$4.3 \cdot 10^{-3}$	[m]
Actuator stiffness	$1.5 \cdot 10^{6}$	[N/m]
Piezoelectric coefficient	$2.6 \cdot 10^{-8}$	[m/V]
Mirror plate		
Diameter	$3.0 \cdot 10^{-2}$	[m]
Thickness h_k	$8.0 \cdot 10^{-4}$	[m]
Young modulus E	$7.2 \cdot 10^{10}$	[N/m^2]
Poison ratio ν	0.17	[-]

with W_0 is piston, W_1 and W_2 are tip and tilt coefficients and:

$$\begin{aligned} W(z,\zeta) = \quad & (z-\zeta)(\overline{z}-\overline{\zeta})\left\{\ln(z-\zeta)+\ln(\overline{z}-\overline{\zeta})+\tfrac{1-\mu}{3+\mu}\cdot\left[\ln(1-z\overline{\zeta})+\ln(1-\overline{z}\zeta)\right]\right\} \\ & +\tfrac{(1+\mu)}{(1-\mu)(3+\mu)}\left\{(1-z\overline{\zeta})\ln(1-z\overline{\zeta})+k(z\overline{\zeta})+(1-\overline{z}\zeta)\ln(1-\overline{z}\zeta)+k(\overline{z}\zeta)\right\} \\ & +\tfrac{(1-\mu)^2}{(1+\mu)(3+\mu)}z\overline{z}\zeta\overline{\zeta} \end{aligned} \tag{3-5}$$

with logarithmic integral:

$$k(x) = \int_0^x \frac{\ln(1-\alpha)}{\alpha}d\alpha = -\sum_{n=1}^{\infty}\frac{x^n}{n^2} \tag{3-6}$$

3-1-4 Actuator to surface profile

It is possible to make a linear model of the surface of the deformable mirror (DM). First a linear relation between input voltages $\mathbf{v}_k$ and the displacements of the actuators due to this voltage input is described (since the model is linear hysteresis is considered not to be present, hysteresis behavior is separately modeled in Chapter 4). This results in:

$$\mathbf{h}_{act} = d_{v,piezo}\cdot\mathbf{v}_k. \tag{3-7}$$

$\mathbf{h}_{act} \in \mathbb{R}^k$ is the linear displacement due to the voltage that is applied to the piezo actuator, $k \in \mathbb{N}$ the number of actuators, $d_{v,piezo} \in \mathbb{R}$ is the piezoelectric coefficient, $\mathbf{v}_k \in \mathbb{R}^k$ is the voltage applied to the piezo actuator. This displacement $\mathbf{h}_{act}$ does not have to be the actual displacement, since the mirror can push back due to internal forces, caused by height differences. The total displacement of actuators points is:

$$\mathbf{h}_k = \mathbf{h}_{act} + \frac{\mathbf{P}_k}{k_{piezo}} \tag{3-8}$$

$\mathbf{h}_k \in \mathbb{R}^k$ is the actual displacement of height at the location of actuator k. This displacement is the result of the voltage applied to that specific actuator and internal

forces pressing or pulling the actuator. $\mathbf{P}_k \in \mathbb{R}^k$ is the internal force vector due to deformation in the mirror. $k_{piezo} \in \mathbb{R}$ is the spring constant of the piezo actuator.
A vector $\mathbf{h}_n$ containing the displacements at N chosen points can be written as a function of internal forces $\mathbf{P}_k$, piston coefficient $W_0 \in \mathbb{R}$ and tip and tilt coefficients $W_1 \in \mathbb{R}$ and $W_2 \in \mathbb{R}$ [8].

$$\mathbf{h}_n = \frac{\mathbf{P}_k}{16\pi D_k} \cdot \mathbf{W}_{grid,n} + W_0 \cdot [11..1]^T + W_1 \cdot \mathbf{x}_n + W_2 \cdot \mathbf{y}_n \tag{3-9}$$

$W_{grid,n} \in \mathbb{R}^{n \cdot k}$ is a matrix constructed by use of equation 3-5, based on the $n \in \mathbb{N}$ evaluated observation points at location z and location of the k point-like forces, located at actuator position ζ. $\mathbf{x}_n$ and $\mathbf{y}_n$ are the coordinates of the observation points in a cartesian grid.
It is necessary to calculate $\mathbf{P}_k$, W_0, W_1 and W_2 first before $\mathbf{h}_n$ can be obtained. The easiest way is first to calculate $\mathbf{h}_k$, the displacements at the actuator locations. It should not be forgotten that there must be a force and momentum equilibrium in the actuator points: $\sum_{i=1}^{k} P_i = 0$, $\mathbf{P}_k \cdot \mathbf{x}_k = 0$ and $\mathbf{P}_k \cdot \mathbf{y}_k = 0$.
Now it is possible to combine these equations and solve them in one operation with help of Gaussian elimination.

$$\begin{bmatrix} \mathbf{h}_{act} \\ \mathbf{0}_k \\ 0 \\ 0 \\ 0 \end{bmatrix} = \mathbf{M} \begin{bmatrix} \mathbf{P}_k \\ \mathbf{h}_k \\ W_0 \\ W_1 \\ W_2 \end{bmatrix} = \begin{bmatrix} \mathbf{I}_k / k_{piezo} & \mathbf{I}_k & 0 & 0 & 0 \\ \frac{\mathbf{P}_k}{16\pi D_k} \cdot \mathbf{W}_{grid,k} & -\mathbf{I}_k & \mathbf{1}_{1 \vdots k} & \mathbf{x}_{1 \vdots k} & \mathbf{y}_{1 \vdots k} \\ 1_1 \; 1_2 \cdots 1_k & 0 & 0 & 0 & 0 \\ x_1 \; x_2 \cdots x_k & 0 & 0 & 0 & 0 \\ y_1 \; y_2 \cdots y_k & 0 & 0 & 0 & 0 \end{bmatrix} \begin{bmatrix} \mathbf{P}_k \\ \mathbf{h}_k \\ W_0 \\ W_1 \\ W_2 \end{bmatrix} \tag{3-10}$$

$$\begin{bmatrix} \mathbf{P}_k \\ \mathbf{h}_k \\ W_0 \\ W_1 \\ W_2 \end{bmatrix} = \mathbf{M}^{-1} \begin{bmatrix} \mathbf{h}_{act} \\ \mathbf{0}_k \\ 0 \\ 0 \\ 0 \end{bmatrix} \tag{3-11}$$

with $\mathbf{M} \in \mathbb{R}^{(2k+3) \cdot (2k+3)}$.

Now $\mathbf{P}_k$, W_0, W_1 and W_2 are obtained, equation 3-9 can be used to calculate $\mathbf{h}_n$, a grid of observation points. This grid can for instance be used for creating pictures that show the shape of the DM (with the $n = 37$ points placed at the actuators it is not possible to give a detailed view of the mirror shape). Or it can be used to create enough points such that an accurate approximation of a desired shape can be found. It is possible to obtain a direct relationship between the input voltage and the heights $\mathbf{h}_n$ of observation points at z. For clarification first $\mathbf{M}^{-1}$ will be split up in different matrices.

$$\mathbf{M}^{-1} = \left[\begin{array}{c|c|c} \mathbf{M}_{inv,1} & \mathbf{M}_{inv,2} & \mathbf{M}_{inv,3} \\ \hline \mathbf{M}_{inv,4} & \mathbf{M}_{inv,5} & \mathbf{M}_{inv,6} \\ \hline \mathbf{M}_{inv,7a} & \mathbf{M}_{inv,8a} & \mathbf{M}_{inv,9a} \\ \mathbf{M}_{inv,7b} & \mathbf{M}_{inv,8b} & \mathbf{M}_{inv,9b} \\ \mathbf{M}_{inv,7c} & \mathbf{M}_{inv,8c} & \mathbf{M}_{inv,9c} \end{array}\right] \tag{3-12}$$

In case the observation points are located at the actuators (heights are denoted by $\mathbf{h}_k$), the answer is straight forward:

$$\mathbf{h}_k = \mathbf{M}^{-1}(k+1:2k, 1:k) \cdot \mathbf{h}_{act} = \mathbf{M}_{inv,4} \cdot \mathbf{h}_{act} \tag{3-13}$$

Combined with equation 3-7, this gives the direct relation between heights at the actuators $\mathbf{h}_k$ and input voltages $\mathbf{v}_k$.

$$\mathbf{h}_k = d_{v,piezo} \cdot \mathbf{M}_{inv,4} \cdot \mathbf{v}_k \tag{3-14}$$

However, it is most likely that not all observation points are located at the place of an actuator. In case that heights at other places then at the locations of actuators are desired, it is still possible to derive a direct relationship between those heights an the input voltages, without first calculating $\mathbf{P}_k$, W_0, W_1 and W_2 and then applying formula 3-9. This can be done by directly combining equation 3-9 and 3-12.

$$\begin{aligned} \mathbf{h}_n &= \tfrac{\mathbf{w}_{grid,n}}{16\pi D_k} \cdot \mathbf{P}_k + W_0 \cdot [11..1]^T + W_1 \cdot \mathbf{x}_n + W_2 \cdot \mathbf{y}_n \\ &= \tfrac{\mathbf{w}_{grid,n}}{16\pi D_k} \cdot \mathbf{M}_{inv,1} \cdot \mathbf{h}_{act} + \mathbf{M}_{inv,7a} \cdot \mathbf{h}_{act} \cdot [11..1]^T \\ &\quad + \mathbf{M}_{inv,7b} \cdot \mathbf{h}_{act} \cdot \mathbf{x}_n + \mathbf{M}_{inv,7c} \cdot \mathbf{h}_{act} \cdot \mathbf{y}_n \end{aligned} \tag{3-15}$$

Since $\mathbf{M}_{inv,3a}$, $\mathbf{M}_{inv,3b}$, $\mathbf{M}_{inv,3c}$, $[11..1]^T$, $\mathbf{x}_n$, $\mathbf{y}_n$ are all one dimensional arrays, it is possible to rearrange equation 3-15.

$$\begin{aligned} \mathbf{h}_n &= \tfrac{\mathbf{w}_{grid,n}}{16\pi D_k} \cdot \mathbf{M}_{inv,1} \cdot \mathbf{h}_{act} + [11..1]^T \cdot \mathbf{M}_{inv,7a} \cdot \mathbf{h}_{act} \\ &\quad + \mathbf{x}_n \cdot \mathbf{M}_{inv,7b} \cdot \mathbf{h}_{act} + \mathbf{y}_n \cdot \mathbf{M}_{inv,7c} \cdot \mathbf{h}_{act} \\ &= (\tfrac{\mathbf{w}_{grid,n}}{16\pi D_k} \cdot \mathbf{M}_{inv,1} + [11..1]^T \cdot \mathbf{M}_{inv,7a} + \mathbf{x}_n \cdot \mathbf{M}_{inv,7b} + \mathbf{y}_n \cdot \mathbf{M}_{inv,7c}) \cdot \mathbf{h}_{act} \end{aligned} \tag{3-16}$$

The direct relationship between voltages and the heights $\mathbf{h}_n$ at z is becomes

$$\begin{aligned} \mathbf{h}_n &= d_{v,piezo} \cdot (\tfrac{\mathbf{w}_{grid,n}}{16\pi D_k} \cdot \mathbf{M}_{inv,1} + [11..1]^T \cdot \mathbf{M}_{inv,7a} + \mathbf{x}_n \cdot \mathbf{M}_{inv,7b} + \mathbf{y}_n \cdot \mathbf{M}_{inv,7c}) \cdot \mathbf{v}_k \\ &= \mathbf{M}_{mirror} \cdot \mathbf{v}_k \end{aligned} \tag{3-17}$$

3-2 Optical path

The shape of (aberrated) wavefront can be described in multiple ways. These methods can be divided into categories: zonal and modal. Both methods will be discussed in the following Paragraphs.

3-2-1 Zonal notation

The zonal notation describes the wavefront at certain coordinates. One way to do so is by simply taking the height of the wavefront at certain coordinates. The wavefront at location (x, y) can be denoted as $h(x, y)$. Sometimes the shape is also written as a function of the wavelength, this is know as the phase change.

$$\phi(x, y) = \frac{4\pi}{\lambda} h(x, y) \tag{3-18}$$

λ is the wave length of the light. Unaberrated wavefront is denoted as ϕ_0, aberrated wavefront as ϕ_{ab} and the wavefront produced by the DM as ϕ_{dm} [4].

3-2-2 Modal notation

With modal notations the shape of the wavefront is decomposed into a summation of different shapes with each a coefficient. In most cases these shapes are chosen to be orthogonal modes of each other. In wavefront correction the Zernike modes are very popular. Another type of orthogonal modes are the Lukosz modes. The Zernike and Lukosz modes are based on the polar coordinate system:

$$h(x, y) = \sum_{i=0}^{k} a_i Z_i(\rho, \theta) \tag{3-19}$$

$Z_i(\rho, \theta)$ is the height of the i^{th} Zernike mode, at polar coordinate (ρ, θ). a_i is the amplitude of mode i. $x = \rho \cdot cos(\theta)$, $y = \rho \cdot sin(\theta)$. When Lukosz modes are used $Z_i(\rho, \theta)$ in formula A-1 is replaced by $L_i(\rho, \theta)$, named the Lukosz mode. As variable for the coefficient, a_i can still be used, but of course its value will change, since it corresponds to a different shape of wavefront. In case of unaberrated wavefront all coefficients will be zero. The coefficients of aberrated wavefront are collected in array $\mathbf{a} \in \mathbb{R}^m$ with m the amount of evaluated Zernike or Lukosz modes. The coefficients of the compensation device are in $\mathbf{b} \in \mathbb{R}^m$ and the corrected wavefront is $\mathbf{c} = \mathbf{a} + \mathbf{b}$. The formulas for calculating Zernike modes, together with a number of Zernike mode shapes are shown in Appendix A.

3-3 Pinhole

In the upcoming Subsection explains how the light intensity behind the pinhole can be calculated. In subsection 3-3-2 the chosen size of the pinhole is motivated.

3-3-1 Intensity after the pinhole

The electromagnetic field of the light beam after in the focal plane of the lens is

$$A(\xi, \eta) = A_0(\xi, \eta) \cdot e^{i(\phi_{ab}(\xi,\eta) + \phi_{dm}(\xi,\eta) + \phi_{lens}(\xi,\eta))} \tag{3-20}$$

where $A_0(\xi, \eta)$ is a constant amplitude. ξ and η form the coordinate system of the light beam, u and v are coordinates that describe the surface of the pinhole. The pattern is called the Fraunhofer diffraction. The intensity at a point P can be described as the square of the Fourier transformation of the pattern. The total intensity measured by the photodiode is the integral over the surface of the intensity points [4].

$$I_{pinhole} = \int \int_{pinhole} |\mathcal{F}\{A(u,v)\}|^2 \, \mathrm{d}u\mathrm{d}v \tag{3-21}$$

3-3-2 Size of the pinhole

The size of the pinhole is important in order to find the best correction possible. If the pinhole is too small, only a small part of the light will travel through the pinhole, and thus different shapes of the DM can lead to the same intensity measured by the photodiode. If the pinhole is too large, the complete focussed beam will travel through the pinhole, no matter it is focussed or not. In both cases it is not possible to measure the best correction [4].
If the pinhole is chosen to have the same size as the first Airy disk, then there is only one shape of PDM that leads to maximum light intensity. The size of the first Airy disk, and the desired pinhole size is: [4]:

$$d = \frac{2.44 \cdot \lambda \cdot f}{D} \tag{3-22}$$

with λ the wavelength, 633 nm, f the focal length, this is 400 mm. D is the diameter of the beam. This diameter is chosen according to [9].
First the number o of low order terms possible to correct is calculated through:

$$K_{tot} = (o^2 + 3o + 2)/2 \tag{3-23}$$

with $K_{tot} = 37$, which gives $o = 7$.
According to [9], for a continuous facesheet DM the number of external actuators (actuators at place where no light is reflected) should satisfy the condition:

$$K_{ext} \geq 4o - 2 \tag{3-24}$$

For the 37 channel DM this leads to $K_{ext} = 30$. The corresponding aperture is 0.3-0.48 times the diameter of the mirror. The aperture is chosen to be 0.4 times the diameter of mirror: 12mm. If the diameter is smaller, there is the possibility that the number of external actuators will be larger. If the diameter is selected larger, inaccurate alignment can lead to the increase of K_{ext}, violating equation 3-24.
Now the parameters are known, the diameter of the pinhole can be calculated.
$d = \frac{2.44 \cdot 633^{e-9} \cdot 400e^{-3}}{12e^{-3}} = 51.5e^{-6}m = 51.5\mu m$
A pinhole of 50 μm is the closest available on the market.

3-4 High voltage amplifier

The used amplifier producing the voltages to drive the PDM was manufactured by Flexible Optical B.V. (OKO® Technologies). The high voltage amplifier (HVA) contains 40 identical amplifiers, with a voltage output range of 0 - 300 volt. However due to increased noise around the upper limit, the voltage range was restricted to 0-290 volts. Channel 18 of the HVA was excited with random signal to identify the characteristics of the amplifier. The output was identified with output error model with parameters $nb = 1$, $nf = 1$ and $nk = 1$. The found transfer function was:

$$\frac{25.16}{z - 0.6882}, \text{ sample time: } 0.0001 \text{ s} \tag{3-25}$$

The corresponding Bode plot of the transfer function is shown in Figure 3-2.

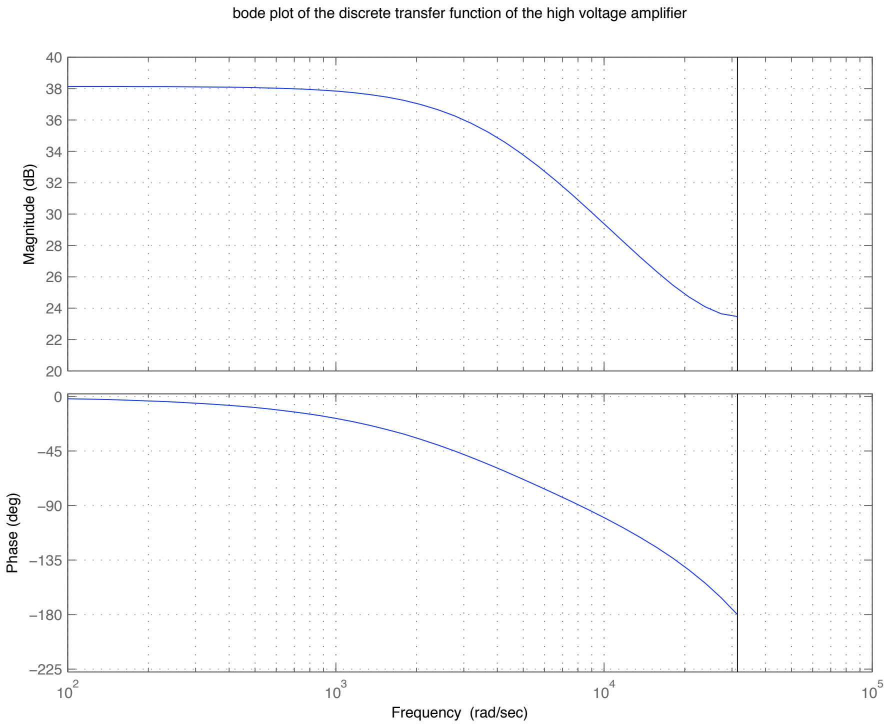

Figure 3-2: Bode plot of the high voltage amplifier, used to drive the PDM in the WFSless AO setup.

Chapter 4

Hysteresis Compensation

In this Chapter the development of a hysteresis compensator is described. After an example of hysteresis in Section 4-1, a method to extract hysteresis curves in a WFSless AO setup will be given in Section 4-2. In Section 4-3 possibilities of modeling hysteresis are discussed. The choice for the Coleman-Hodgdon equation is motivated in Section 4-4, together with elaboration on its formulas. Identification of parameters of this model is done in Section 4-5. The performance of the hysteresis compensator will be evaluated in Section 4-6, followed by conclusions in Section 4-7.

4-1 Hysteresis of piezo actuators

The deformable mirror (DM) is actuated by 37 piezo-electro tubes that push or pull the surface of the mirror. As already described in Section 2-2-4, downside of piezo-electro material is that it suffers from hysteresis when actuated. The stroke and force produced, is not only dependant on the voltage, but also on whether the voltage is increasing or decreasing and from which point this change of direction occurred. This is clearly visible in Figure 4-1: if only x is known, nothing can be said about the value of y. In this example where x is moving between two extremes, $x = 0$ can already have three answers: a, b or c. If x decreases before y reaches its minimum or maximum, y can have any value between a and c. To know more about the location, more information or other data is needed. In general, it can be said that in the case of the piezo actuator the relation between voltage and stroke is not linear.
This behavior reduces the accuracy and bandwidth of the system. If an inverse model of this hysteresis can be found, the influence of hysteresis can drastically be reduced and better performance can be obtained.

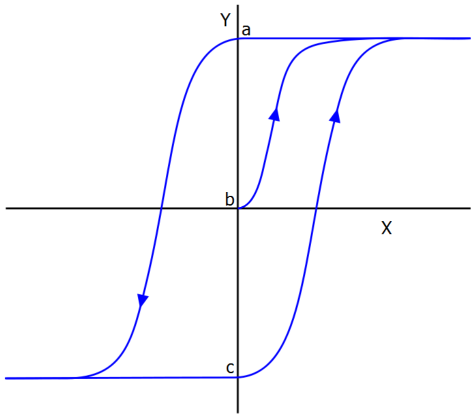

Figure 4-1: An example of hysteresis.

4-2 Extracting hysteresis curves in a WFSless AO setup

In traditional AO system where the wavefront is reconstructed, it is possible to calculate the height of the mirror at certain points. With these heights the relation between the height and the voltage sent to a certain actuator can easily be described, making it possible to obtain hysteresis curves.

Since in the used setup no wavefront recording device is present, an other method has to be used to obtain the hysteresis pattern. H. Song developed a method based on the Foucault knife test [10]. In this test light coming from the DM was focussed on the edge of a razor blade which partially blocked the light. The light that passed the blade generated a voltage in a photodiode. This is graphically represented in Figure 4-2.

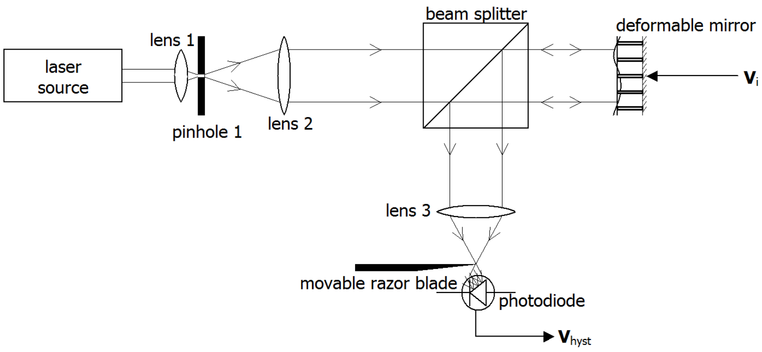

Figure 4-2: Schematics of the Foucault knife test. The input voltage is denoted by $\mathbf{v}_i$; output voltage is light intensity measurement $\mathbf{v}_{hyst}$.

The voltage produced by the photodiode, $\mathbf{v}_{hyst}$, is described according to following equation:

$$\mathbf{v}_{hyst} = A \int\int_{\Sigma} |\int\int_{-\infty}^{\infty} e^{-j(\phi_{ab}(\xi,\eta)+\phi_{dm}(\xi,\eta))} \cdot e^{-j\frac{1}{f}(u\xi+v\eta)} \mathrm{d}\xi \mathrm{d}\eta|^2 \mathrm{d}u\mathrm{d}v \qquad (4\text{-}1)$$

where A is a constant depending on the setup, j is $\sqrt{-1}$, λ is the wavelength, f the focal distance of the lens, (ξ, η) the coordinates of the input light plane and (u, v) the coordinates in the focal plane of the lens. ϕ_{ab} represents the wavefront of the initial aberration present in the setup; ϕ_{dm} is the wavefront produced by the DM. Σ describes the area that is not blocked by the razor knife. The method of extracting hysteresis curves with help of the Foucault knife edge test is possible to implement in the experimental setup and is used to do so.

In order to obtain information about the hysteresis, an oscillating signal $\mathbf{v}_i$ is applied to an actuator. This signal will change the voltage $\mathbf{v}_{hyst}$ produced by the photodiode. The relation between the input voltage $\mathbf{v}_i$ and the voltage $\mathbf{v}_{hyst}$ from the photodiode depends on the actuator, which is actuated, and the position of the razor blade. $\mathbf{v}_{hyst}$ can be non-linear (as can be expected from equation 4-1). Objective of this test is to find a signal $\mathbf{v}_{hyst}$ coming from the photodiode that has the largest possible amplitude (for a good SNR), while the several up- and down-going branches are clearly distinguishable from one another. Finding this signal is an iterative process, in which different actuators are tested and the razor is tuned to get a proper signal. As actuation signal a triangular signal was used, because the earlier used sinusoid signals gave less sharp points at the edges of the curves. Creep present in the actuators was considered to be linear through time and thus could be subtracted.

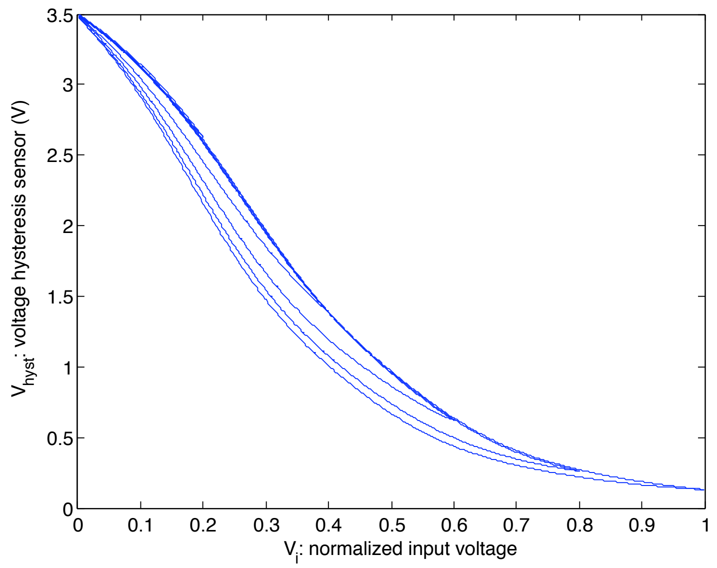

Figure 4-3: Extracted hysteresis curves of actuator 9 after creep was subtracted.

In the used WFSless AO setup, all actuators where evaluated in order to find hysteresis curves. Not all actuators gave a useful signal. Sometimes the amplitude was too low, other times the difference between the different hysteresis branches was not clearly visible. Actuator 9 gave a particularly good signal, visible in Figure 4-3, and was therefore used for identification. This curve is however non-linear. For hysteresis modeling the curve should be normalized: the hysteresis branches should run from point $[0, 0]$ to $[1, 1]$. In order to obtain this, the input sequence with the largest amplitude should begin at 0 and end at 1. For the hysteresis curve of Figure 4-3 it is not exactly known how the curve would behave, when there is no hysteresis present. Song [10] proved that taking the average of the largest up-going $\mathbf{v}_{hyst\_up}$ and down-going branch $\mathbf{v}_{hyst\_down}$ gives a good approximation. This average will be called $\mathbf{v}_{hyst\_avg}$. It is now possible to describe the non-linear relation between $\mathbf{v}_i$ and $\mathbf{v}_{hyst\_avg}$ as following:

$$\mathbf{v}_{hyst\_avg} = F(\mathbf{v}_i) \tag{4-2}$$

It is trivial that by taking the inverse of $F(\mathbf{v}_i)$ and plotting the line $\mathbf{v}_i$ versus $F^{-1}(\mathbf{v}_{hyst\_avg})$, the inverse function, would result in a straight line running from 0 to 1. However, this can also be done for the case where $\mathbf{v}_{hyst\_avg}$ is replaced by $\mathbf{v}_{hyst\_up}$ and $\mathbf{v}_{hyst\_down}$. This immediately reveals a hysteresis curve beginning in 0 and ending in 1, since $\mathbf{v}_{hyst\_avg}$, $\mathbf{v}_{hyst\_up}$ and $\mathbf{v}_{hyst\_down}$ all start or end in the origin or $[1, 1]$. The easiest way to find inverse function F^{-1} is to make polynomial fit of $\mathbf{v}_i = F^{-1}(\mathbf{v}_{hyst\_avg})$. This is done as follows:

$$\hat{v}_i = F^{-1}(\mathbf{v}_{hyst\_avg}) = \sum_{l=-1}^{11} a_l \mathbf{v}_{hyst\_avg}^l \tag{4-3}$$

where:

$$a_l = \arg\min_{a_l}\Big(\sum_{l=-1}^{11} a_l \mathbf{v}_{hyst\_avg}^l\Big) - \mathbf{v}_i \tag{4-4}$$

In Figure 4-4 the result of identifying the inverse is shown. After identifying the inverse

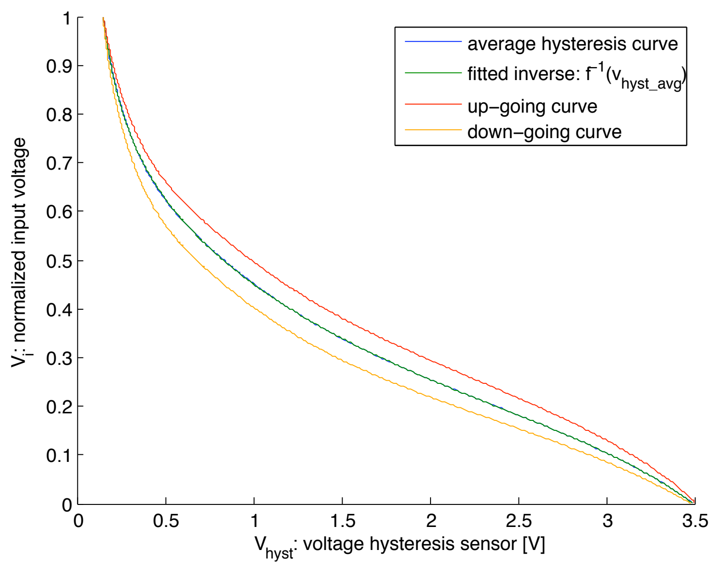

Figure 4-4: Identification of the inverse hysteresis curve of actuator 9, needed to create the normalized hysteresis curve (Figure 4-5).

function, the up- and down-going hysteresis curves can also be transformed.

$$\mathbf{v}_{hyst\_norm} = F^{-1}(\mathbf{v}_{hyst}) = \sum_{l=-1}^{11} a_l \mathbf{v}_{hyst}^l \tag{4-5}$$

The result of this transformation can be seen in Figure 4-5.

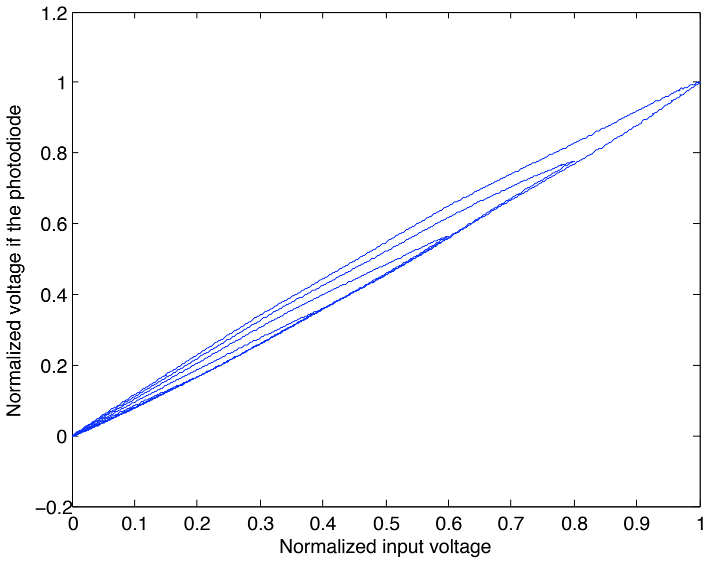

Figure 4-5: Normalized hysteresis curve of actuator 9, running between [0,0] and [1,1].

4-3 Modeling hysteresis

There are basically three ways of hysteresis compensation (HC) for piezo electric actuators: (1) charge control [11], (2) feedforward control [12][13][14] and (3) feedback linearization [15]. Song [16] notes that charge control reduces the sensitivity of displacement and additional hardware is required. Feedback linearization requires a sensor for each actuator. This is costly and can sometimes be impossible in terms of space required by the sensors. Last option is feedforward control, which can compensate hysteresis without extra hardware. Since this thesis tries to keep the amount of hardware in the WFSless AO setup at a minimum, this option is the ideal choice. Less hardware, means less costs and makes the AO less expensive.

In feedforward control there are multiple methods of describing the hysteresis model. These different methods will be described in the upcoming Paragraphs. The most often mentioned methods for compensating hysteresis in DMs are based on the Preisach model framework combined with a function or look-up table for the weights. The Coleman-Hodgdon equations (short referred as C-H eq.) are far less used. Last method being mentioned describes hysteresis behavior with polynomial functions.

4-3-1 Polynomial functions

Polynomial functions can give good results for repetitive curves. However, if the control inputs are more complex, like an input that contains multiple frequency components or input with changing amplitudes, the polynomial function is not able to describe the hysteresis curve correctly. This can lead to significant errors according to Croft [13]. Therefore, this method is not used in this research.

4-3-2 Preisach model

The Preisach model is a framework that models hysteresis as a series of switches. The switches have a lower threshold β and an upper threshold α. The switch has the following value:

$$y(x) = \begin{cases} 0 & \text{if} \quad x < \beta \\ 1 & \text{if} \quad x > \alpha \\ k & \text{if} \quad \beta < x < \alpha \end{cases} \tag{4-6}$$

$k = 0$ if x had a value $\leq \beta$ before it passed a threshold for the last time. $k = 1$ if x had a value $\geq \alpha$ before it passed a threshold for the last time. This is represented in Figure 4-6.

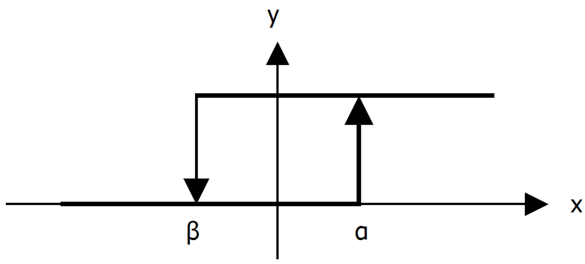

Figure 4-6: Relay hysteron, which switches to a high value if α is passed and only switches back is the value on the x axis is lower then β.

The discrete Preisach model, consists out of multiple switches. Each switch is multiplied with a value μ. The result consists out of a summation of every μ multiplied with the value of the switch. This is graphically show in Figure 4-7.

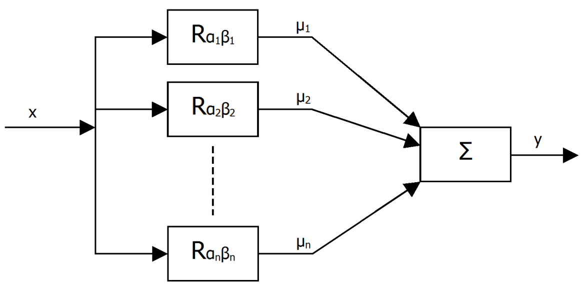

Figure 4-7: Preisach model consisting of parallel switches. The summation of output of the switches models the hysteresis curves.

The discrete Preisach performs better in terms of following the hysteresis curves, if the number of switches is increased. Weight μ is depending on values of α and β. These values can be found through identification or fitting of real-life data. $\mu(\alpha, \beta)$ can be saved in a look-up table or can be calculated with a function which has input variables α and β. The Preisach approach is capable of modeling the hysteresis very well for inputs of different inputs [13]. Dubra [14] states that a system can be controlled with a limited number (10-15) of variables. Song [16] was able to compensate hysteresis present in a PDM with the help of the Preisach network. The hysteresis curves were identified with a neural network and with hinging hyperplanes.

4-3-3 The Coleman-Hodgdon equations

The Coleman-Hodgdon equations give the possibility to describe the hysteresis curves with even less amount of parameters (5-8) than the Preisach network. In the past HC with the help of the C-H eq. for a deformable mirror was achieved by Yang [17]. This was based on the improved C-H eq. by Dirschl [18]. This method makes use exponential functions to describe the hysteresis.

$$x_{\pm}(V) = [A - Bexp(-CV_R)]V \mp D \times [1 - \frac{2}{exp(\mp EV_m) + exp(\mp EV_M)} \times exp(\mp EV)] + F \tag{4-7}$$

$V \in \mathbb{R}$ is the actual voltage applied to the piezo component. $V_M \in \mathbb{R}$ is the maximum voltage on the curve (local maximum), $V_m \in \mathbb{R}$ the minimum voltage (local minimum). Voltage range is defined as $V_R = V_M - V_m$. Variables A to $F \in \mathbb{R}$ can be determined with help of a least square optimization that fits the variables on the obtained data set.

4-3-4 Choice of compensation model

Because of the mentioned disadvantages, polynomial functions are not possible to use for HC. This leaves only the Preisach network and the Coleman-Hodgdon equations. Within AO section of DCSC there is much experience with the Preisach network, however the C-H eq. remain relatively uninvestigated. The limited number of parameters of the C-H eq. makes it an interesting alternative. Besides, there was suspicion that the C-H eq. can work with even less parameters and that there are other possibilities of finding an inverse-hysteresis model with the C-H eq. This will be discussed in the upcoming Section. To sum it up, the C-H eq. look like a promising alternative. That is why this method is chosen for compensation of hysteresis.

4-4 Hysteresis modeling with the Coleman-Hodgdon equations

For feed-forward control of the deformable mirror with the Coleman-Hodgdon equations the inverse of equation 4-7 is needed, so that the appropriate voltage is calculated for a requested elongation of an actuator. This can be done with the help of the Lambert W function.

$$V(x) = \frac{x - a_1}{a_2} - \frac{1}{a_4} W\{\frac{a_3 a_4}{a_2} exp[\frac{a_4(x - a_1)}{a_2}]\} \tag{4-8}$$

$$\begin{aligned} a_1 &= F \mp D \\ a_2 &= A - Bexp(-CV_R) \\ a_3 &= \pm \frac{2D}{exp(\mp EV_m) + exp(\mp EV_M)} \\ a_4 &= \mp E \end{aligned} \tag{4-9}$$

$$W(x) \text{ is the solution to } w \cdot exp(w) = x \tag{4-10}$$

There is also another way of obtaining the inverse model. This is by identifying directly the inverse model as an C-H eq. (so simply switching x and V for the identification). Yang [17] obtained this inverse by the use of formulas 4-8, 4-9 and 4-10, a laborious procedure, which constantly asks for recalculation of the coefficients of formula 4-9 in case V_m or V_M changes and also uses the Lambert W function, which might not be available for every operating platform. This led to an investigation whether it was possible to make a formula $V = f(x)$ based on the form of formula 4-7. The following result was achieved:

$$V_{\pm}(X) = [A + Bexp(-CX_R)]X \pm D \times [1 - \frac{2}{exp(\mp EX_m) + exp(\mp EX_M)} \times exp(\mp EX)] + F \tag{4-11}$$

With this formula it is possible to describe the inverse hysteresis shape immediately, without constantly recalculating the coefficients. When a closer look is taken at formula 4-11, it can be seen that this formula consists out of three parts. First a left side containing variables A, B and C, producing a straight line, which depends on the difference between the local minimum and local maximum. Secondly a middle part that contains the shape of the curve connecting the local minimum and local maximum, using parameters D and E. The last part of the equation is vertical offset, variable F. However there is information about the hysteresis curve, which can reduce the number of variables needed. The normalized inverse hysteresis curve are defined as one running from [0,0] to [1,1]. The shape of this curve is defined by variables D and E. The straight line and offset, which are needed, will let the curve run between [0,0] and [1,1]. These variables can actually be calculated with help of the global maximum (1) and global minimum (0), together with the corresponding voltages (1 and 0). If a new local minimum or maximum is created, the corresponding voltage are already known, based on parameters D and E and information from the past. Now the straight line with the offset can be added, which lets the curve run between its new minimum and maximum.

Thus there is no need to identify parameters A, B, C and F. This simplifies equation 4-11 to the following:

$$V_{\pm}(X) = \begin{array}{l} A(X_M, X_m, V_M, V_m, D, E)X + F(X_M, X_m, V_M, V_m, D, E) \\ \pm D \times [1 - \frac{2}{exp(\mp EX_m) + exp(\mp EX_M)} \times exp(\mp EX)] \end{array} \tag{4-12}$$

where X_M is the current local maximum, V_M is the corresponding voltage of this point, X_m is the current local minimum, V_m is the voltage at this point. As mentioned before, D and E define the shape of the inverse hysteresis curve. D defines the amplitude of the curve. If $D = 0$, then the up-going and down-going line would lie on the line $X = V$. This effect can be observed in the left part of Figure 4-8. An increase of the variable E leads to the ascending inverse hysteresis curve moving to the left as well as an increase in the amplitude of the curve. This behavior is shown in the right part of Figure 4-8.

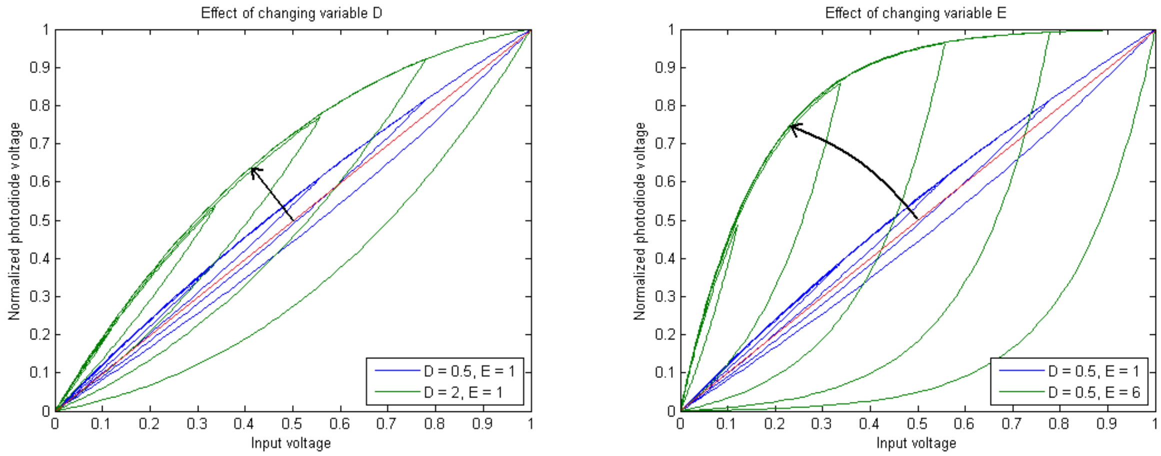

Figure 4-8: Influence of parameters D and E in the Coleman-Hodgdon equations. Left: the effect of changing variable D, this effects the amplitude of the inverse hysteresis curves. Right: effect of changing variable E. This leads to a change of the shape of the hysteresis curve.

4-5 Identification

The anti-hysteresis model was identified with a non-linear least squares algorithm. In order to speed up the convergence and to increase the chances of obtaining the best answer, initial conditions are needed.

In Section 4-3, equation 4-12, it is visible that the anti-hysteresis curve consists out of only two variables: D and E. First, an initial estimation for E needs to be found, since this parameter determines the shape of the curves. After that, an estimation of parameter D is made, which is going to result in a curve, approximating the anti-hysteresis curve. An easy way of finding the shape of the inverse hysteresis, is by plotting $\mathbf{v}_{hyst}$ versus $\mathbf{v}_i - \mathbf{v}_{hyst}$. This results in a curve, starting in the origin $[0, 0]$ and ending in $[1, 0]$. The same is done for the inverse hysteresis model, only for different values for E, the result of this is shown in Figure 4-9. Thus a value of E, which resembles the shape the best, is chosen. The original signal is quite noisy, but a value of 2 for E promises to be a good value for an initial condition. Now an initial estimation

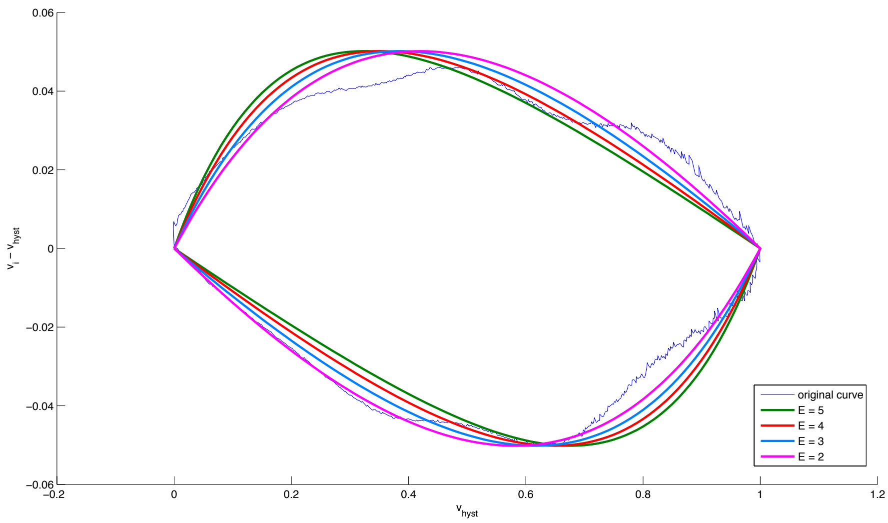

Figure 4-9: Curves for different values of variable E, in order to choose an initial value of E.

of D can be made, by dividing the height of the peak of the original curve by the height of the peak of the anti-hysteresis model:

$$\hat{D} = \frac{\max(abs(\mathbf{v}_i - \mathbf{v}_{hyst}))}{\max(abs(\mathbf{v}_i - \mathbf{v}_{hyst\_model}))} \tag{4-13}$$

Next, different loops are be identified with the non-linear least squares algorithm. First, the up-going curve will be characterized with the initial values of D and E, since all loops will follow this curve while their voltage is increased. This results in values of $D = 0.01231$ and $E = 2.08$.

The downward curves were identified separately, due to the fact that during identification the suspicion occurred that parameter D is dependent on the difference between the local minimum and local maximum of the input voltage V_R, with $V_R = V_M - V_m$. All branches were identified separately. This showed that D could be written as

$$\hat{D} = A - B \cdot exp(C \cdot V_R) \tag{4-14}$$

Optimization gave as answers: $A = 0.085$, $B = -0.33$ and $C = 2.64$.

4-6 Experimental results hysteresis compensation

To investigate the effect of the HC, tests were performed. Three types of tests were done. First the Foucault knife edge test where only one actuator is excited at the time. Second test is the intensity after the pinhole, if only one actuator is activated. Last test measures the intensity after the pinhole, if a triangular signal is applied to the coefficient of one Zernike mode. This last test actuates all actuators to reproduce a

desired shape. The first two tests were performed with actuators which had such a shape that the effect of hysteresis was clearly visible and the SNR was good. This was the case for actuators 1, 9 and 15. To these actuators two different signals were applied: a triangular signal and a random sequence.
If the HC works perfect, the blue area of the system without compensation will turn into a single red line. This means that the uncertainty is totally removed. In practice this did not happen; the compensation reduced the effects of hysteresis, but could not totally remove the uncertainty. The effect of hysteresis compensation can be seen in Figure 4-10. The blue area is drastically reduced into the red area, representing the situation where HC is switched on. It needs to be mentioned that the HC for all actuators is based on the hysteresis curve of actuator 9.

The ideal case for identification would be if the hysteresis could be identified with the help of the light intensity after the pinhole instead of using the Foucault knife edge test. In the second test, Figure 4-11, light intensity after the pinhole is shown. In the case of actuators 1 and 9, the curves do not have a good shape that can be used to identify hysteresis, for voltages larger than 0.3, the curves get too close to one another to make a clear distinction. The shape of curve 15 gets really close to the desired shape, except for the fact that the inverse shape of the curve cannot be approximated with a polynomial function for voltages between 0 and 0.15.

Thus identification of the hysteresis curves seems to be possible with help of the pinhole intensity, but the researcher needs to have "luck" that one of the actuators will produce a usable signal. This luck depends on the layout and parameters of the AO setup and its components. If a non-usable signal is found, the Foucault knife edge test provides a simple and cost effective alternative, which does not require much modifications to the setup and extra components.

The last test, measuring the light intensity after the pinhole when a triangular signal is applied to a Zernike mode, gives insight into the way shape optimization can benefit from HC. In Figures 4-12 and 4-13 it is clearly visible that the usage of Zernike modes is drastically limited by hysteresis. For increasing and decreasing values of the Zernike mode coefficient two different, clearly distinguishable curves emerge. For increasing values a curve with a maximum at the right emerges, for decreasing values a curve with a maximum at the left. This has consequences for future optimization algorithms. A found maximum value on the right curve cannot be found back at the same place as in the left curve. Optimization algorithms can really benefit from hysteresis compensation, which theoretically will lead the two curves merge to one. It can be seen in Figures 4-12 and 4-13 that from the twelve examined the curves, eight modes coincide when hysteresis is compensated. For the other four modes the benefits of HC is less, but it never leads to worse results.

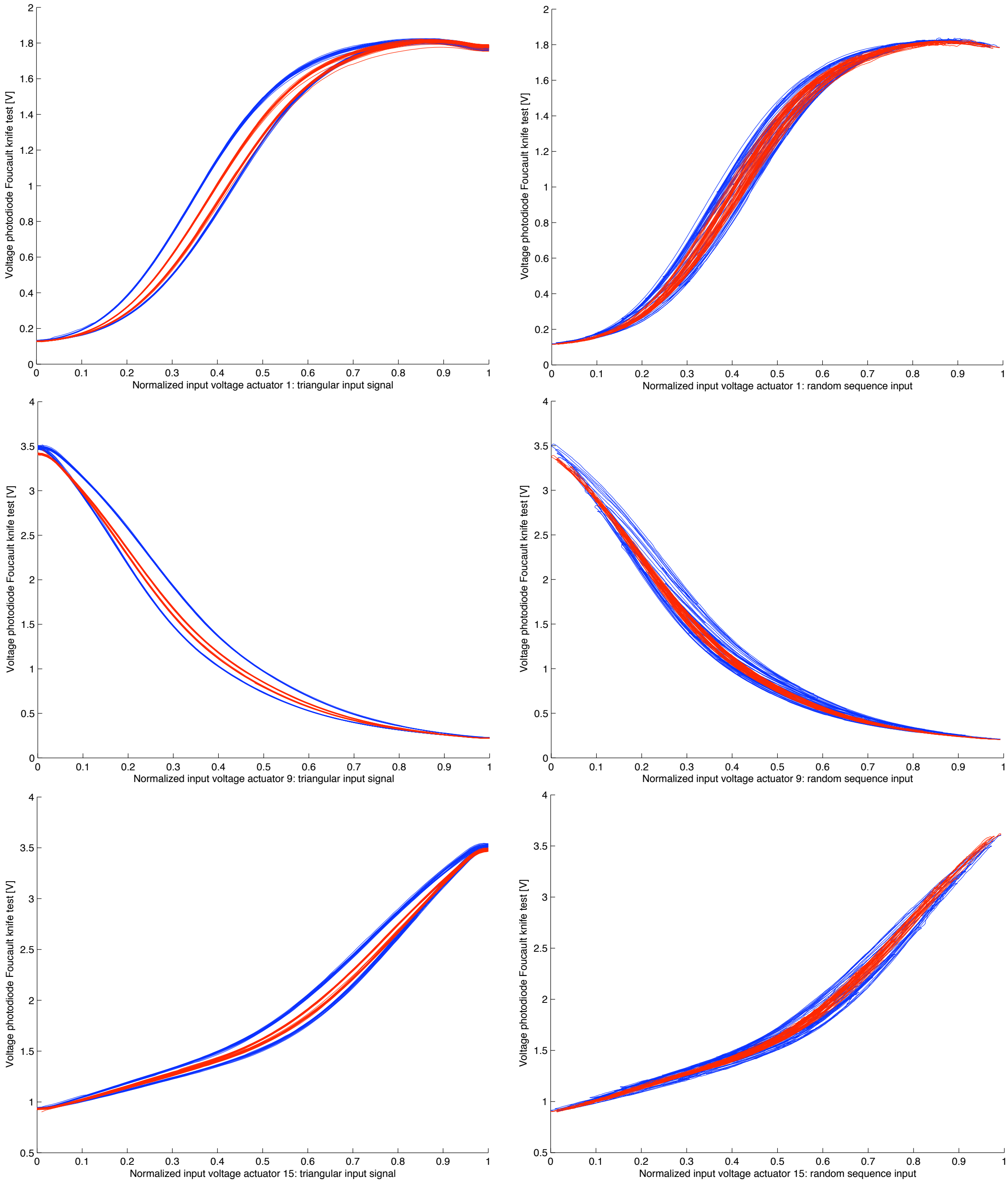

Figure 4-10: Light intensity for individual actuator excitation of actuators 1, 9 and 15, while using the Foucault knife edge test. Blue lines: without hysteresis compensation, red lines: with hysteresis compensation

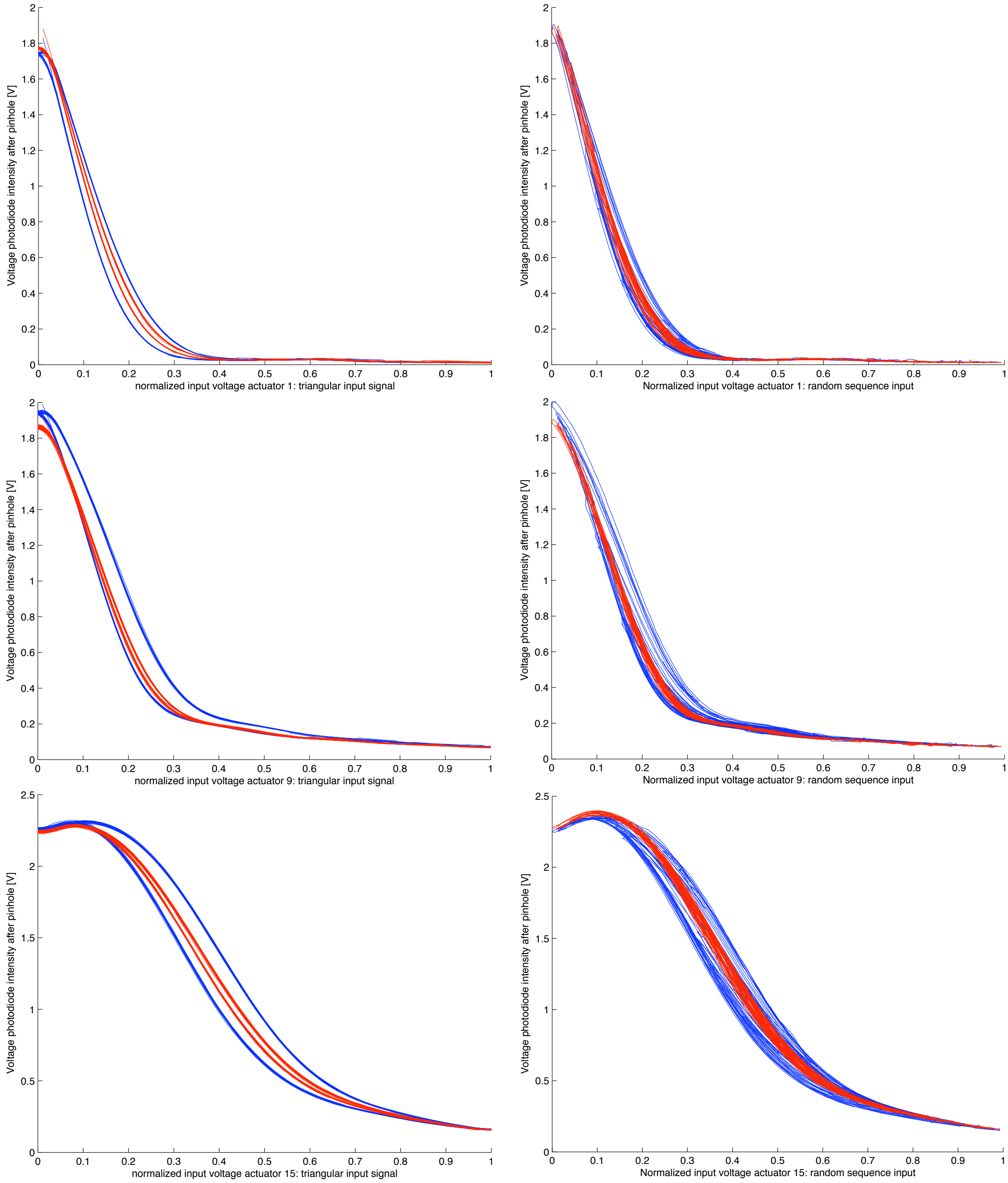

Figure 4-11: Light intensity after the pinhole for individual actuator excitation of actuators 1, 9 and 15. Blue lines: without hysteresis compensation, red lines: with hysteresis compensation

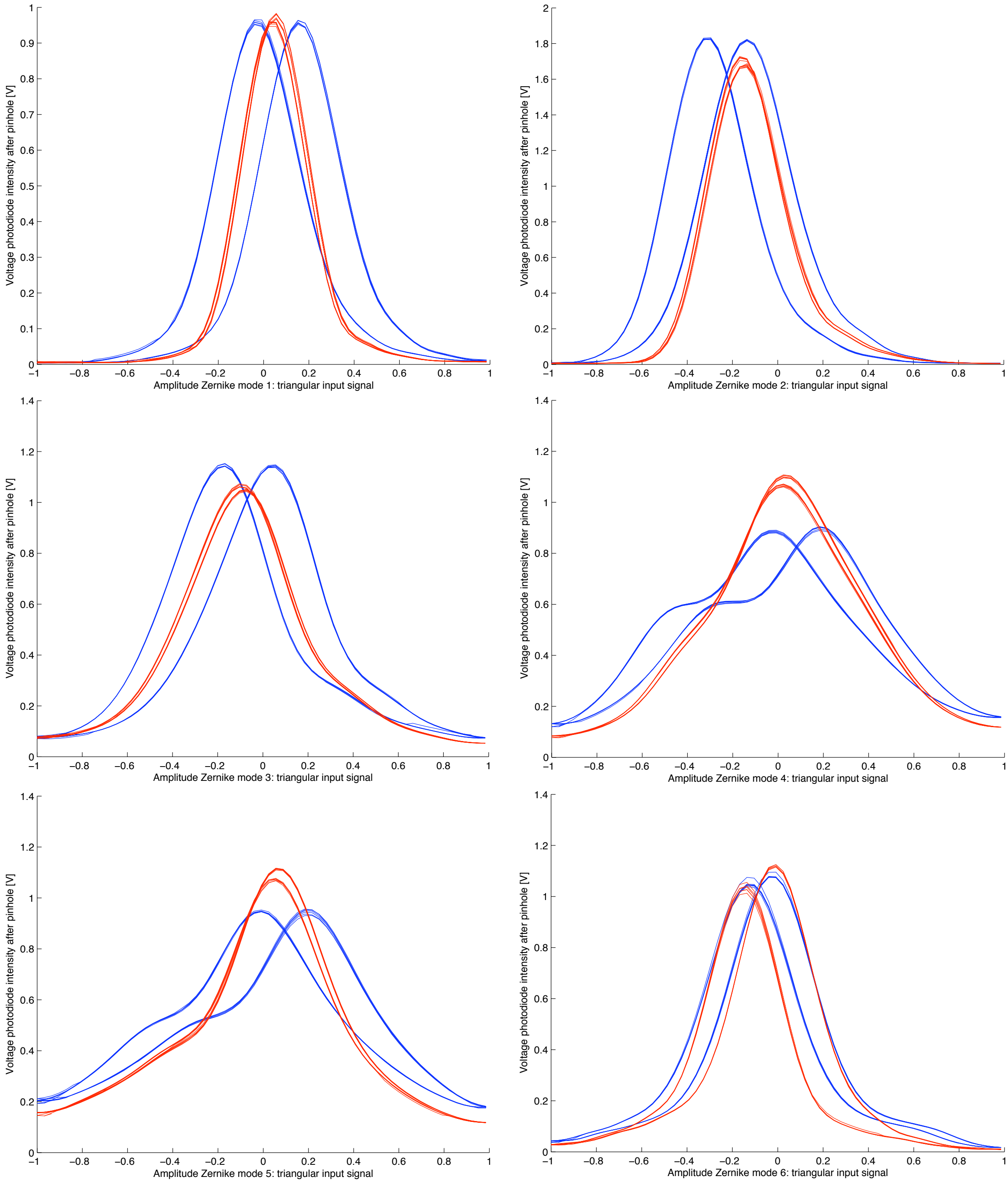

Figure 4-12: Light intensity after the pinhole for individual excitation of Zernike modes 1-6. Blue lines: without hysteresis compensation, red lines: with hysteresis compensation

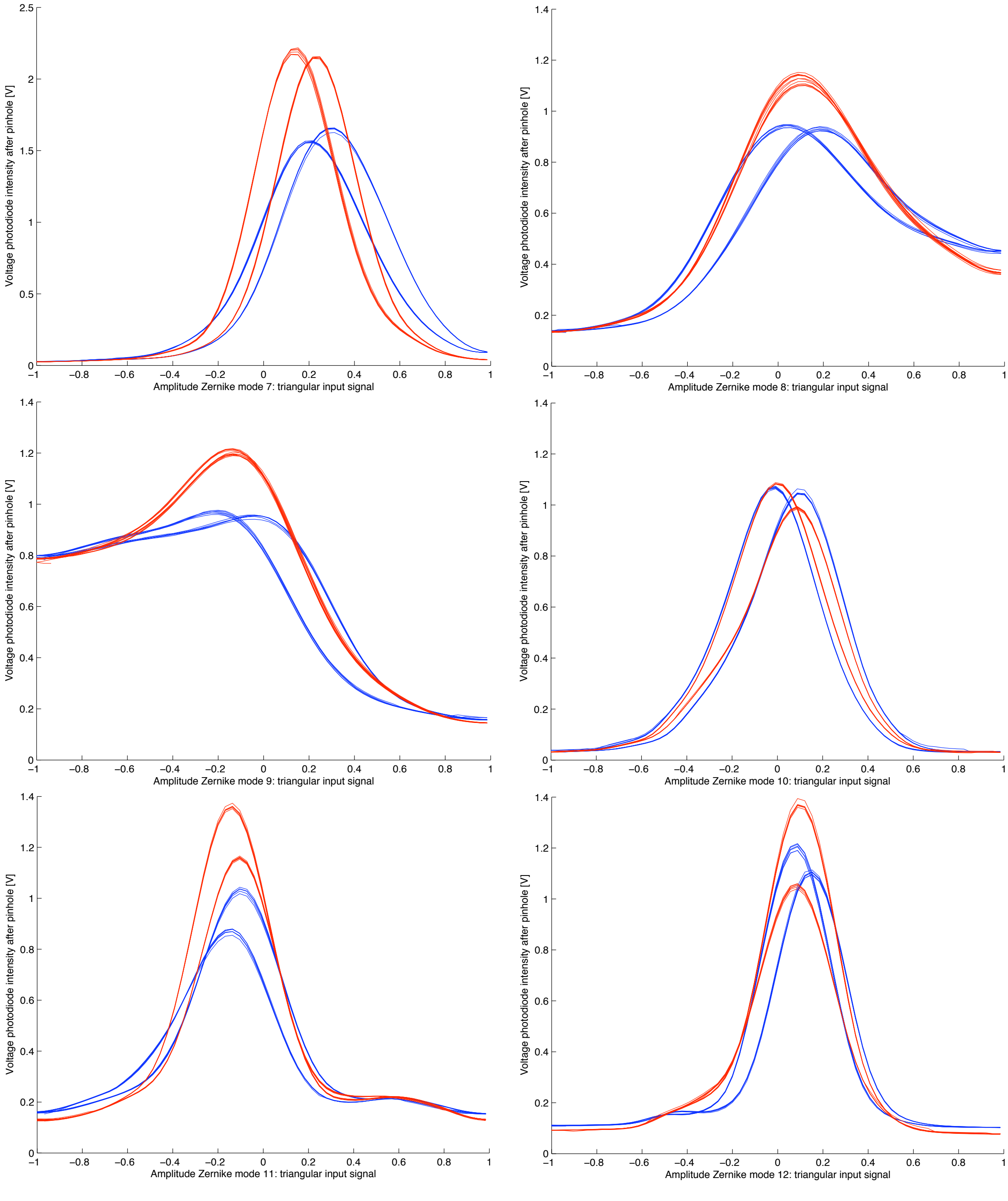

Figure 4-13: Light intensity after the pinhole for individual excitation of Zernike modes 7-12. Blue lines: without hysteresis compensation, red lines: with hysteresis compensation

4-7 Conclusion

It can be concluded that in WFSless AO it is possible to identify HC with the help of the Foucault knife edge test. There is ground for the suspicion that under certain circumstances it should be possible to obtain an inverse hysteresis model while only using the light intensity after the pinhole, bringing the number of components present in a WFSless AO setup to an absolute minimum.
It is shown that HC found for a particular actuator can also reduce the effects of hysteresis for other actuators.
While applying Zernike modes to the PDM, HC improves the chance of finding back the obtained optimum, since HC forces the different shapes of cost functions for ascending and descending amplitudes of some modes to merge to one cost function.

Chapter 5

Optimization Algorithms WFSless AO

In the past WFSless OAs have been developed, although only few were experimentally tested in combination with a pinhole and photodiode as sensor. De Boer [4] and Vdovin[5] used OAs where only the light intensity measured by a photodiode was used as input signal. Booth [19] and Debarré [20] used cameras to minimize optical aberrations. Simulations of WFSless OA were performed by Grisan [21] and Booth [22].
This Chapter explains the optimization algorithms (OA), which will be used to find the best compensation for the aberration, present in the setup.

5-1 Differences in OAs

The goal of the OAs is to maximize the intensity after the pinhole, which implies getting a voltage as high as possible from the photodiode, placed directly after the pinhole. The OAs can be categorized in different classes, divided in the way they search for maximum light intensity. Basically there are two ways optimization can be achieved: with a black-box approach and a modal-driven approach.

A black-box optimization algorithm directly controls the voltages of the mirror. The algorithm does not know anything about the corresponding shape. Advantage of the black-box method is that it does not require a model of the mirror, so it does not suffer from modeling errors as well.

With the modal-driven algorithms, the shape of the DM is optimized. As mentioned in Section 3-2, it is possible to describe wavefront with help of orthogonal modes, like Zernike modes and Lukosz modes. Advantage is that the origin of some aberrations is directly related to some of the modes. Typical examples are tip, tilt and defocus. This means that an OA that optimizes the coefficients of modes, will have an advantage and is likely to find compensation for these parts of the aberration faster. Downside of these modal optimizations is that they heavily rely on the model that describes the surface shape-voltage relation. If the model is not correct, convergence takes longer, or it can happen that the algorithm is even not able to find the optimum at all.

5-2 Black-box optimization

In the past research has been done on OAs for WFSless AO in setups where only the light intensity was measured. [5][4] OAs that perform black-box optimizations, only controlled voltages. Among these OAs were genetic algorithms, simulated annealing and simplex methods. The simplex method gave on overall the best performance, and will be, because of that, the only OA tested in black-box optimization. From now on black-box optimization will be called voltage optimization (VO).

5-2-1 Nelder Mead Simplex

The Nelder-Mead simplex (NM) [23][4] uses only function values, while searching for a minimum. This implies that negative function values must be passed to the algorithm in order to find the maximum:

$$\mathbf{x}^* = \arg\min_{\mathbf{x}} f(\mathbf{x}, \phi_{ab}) \tag{5-1}$$

with $\mathbf{x}^*$ a vertex, containing the voltages and $f(\mathbf{x}, \phi_{ab}) = -I_{photo}$, the negative of the voltage measured by the photodiode. Each function value is connected to a surface shape, produced by applied actuator voltages. The actions taken by the algorithm are described below [23]:

0: initialization

Before start-up four parameters need to be defined to complete the Nelder-Mead method: reflection (ρ), expansion (χ), contraction (ψ) and shrinkage (σ). The standard choice [23][4] for the values of these parameters are:

$$\rho = 1 \qquad \chi = 2 \qquad \psi = \tfrac{1}{2} \qquad \sigma = \tfrac{1}{2} \tag{5-2}$$

An initial guess $\mathbf{x}_1$ is made and a $k+1$ dimensional simplex is constructed around it, with k the number of actuators, in this case 37. An example of this simplex for the two dimensional case ($k = 2$) is given in Figure 5-1. The initial (dashed) simplex contains voltage points $\mathbf{x}_1, \mathbf{x}_2, \ldots \mathbf{x}_{k+1}$.

Now the optimization process begins.

1: order

Order and rename the vertices such that the corresponding function values are sorted like:

$$f(\mathbf{x}_1) \leq f(\mathbf{x}_2) \leq f(\mathbf{x}_3) \leq \ldots \leq f(\mathbf{x}_{k+1}) \tag{5-3}$$

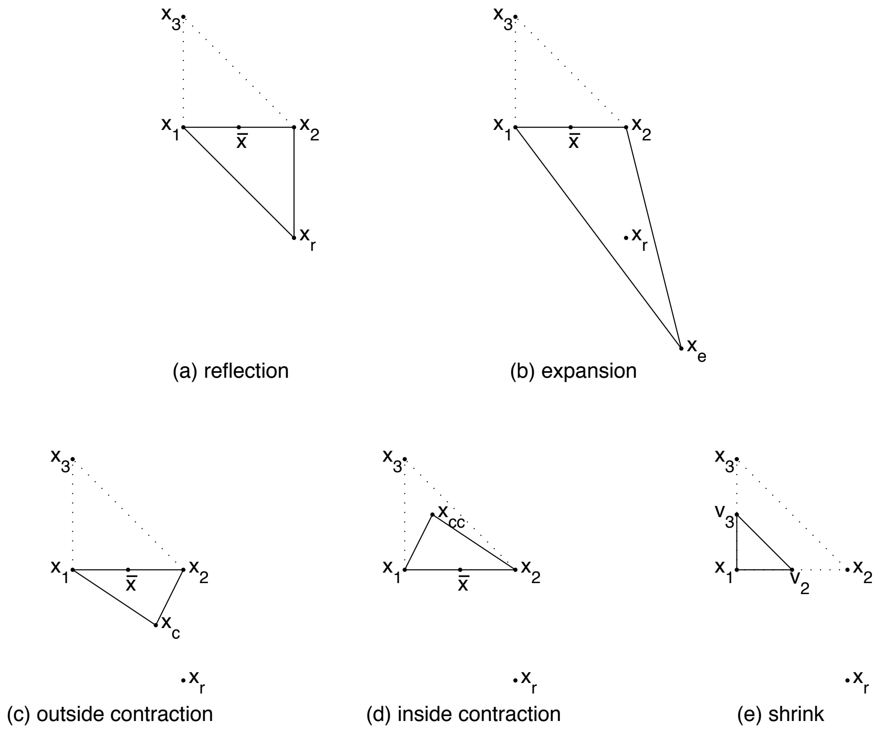

Figure 5-1: Possible simplex transformations performed by the Nelder-Mead optimization algorithm.

Calculate the centroid of the k best points $(\mathbf{x}_1 \ldots \mathbf{x}_k)$.

$$\bar{\mathbf{x}} = \sum_{i=1}^{k} \frac{\mathbf{x}_i}{k} \tag{5-4}$$

2: reflect
Compute reflection point $\mathbf{x}_r$:

$$\mathbf{x}_r = \bar{\mathbf{x}} + \rho(\bar{\mathbf{x}} - \mathbf{x}_{k+1}) = (1+\rho)\bar{\mathbf{x}} - \rho\mathbf{x}_{k+1} \tag{5-5}$$

Apply $\mathbf{x}_r$ as voltages to the DM. This operation is shown in Figure 5-1(a).
Obtain and evaluate $f(\mathbf{x}_r)$. If $f(\mathbf{x}_1) \leq f(\mathbf{x}_r) < f(\mathbf{x}_k)$, then accept $\mathbf{x}_r$ and add it to the simplex and continue at point **1**. If $f(\mathbf{x}_r) < f(\mathbf{x}_1)$ then go to point **3** and perform an expansion. If $f(\mathbf{x}_r) \geq f(\mathbf{x}_k)$, go to point **4** and perform a contraction.

3: expansion
Calculate expansion vertex $\mathbf{x}_e$:

$$\mathbf{x}_e = \bar{\mathbf{x}} + \chi(\mathbf{x}_r - \bar{\mathbf{x}}) = \bar{\mathbf{x}} + \rho\chi(\bar{\mathbf{x}} - \mathbf{x}_{k+1}) = (1+\rho\chi)\bar{\mathbf{x}} - \rho\chi\mathbf{x}_{k+1} \tag{5-6}$$

This expansion step of the is depicted in Figure 5-1(b) with the solid lines.
Obtain and evaluate $f(\mathbf{x}_e)$. If $f(\mathbf{x}_e) < f(\mathbf{x}_r)$ then accept vertex $\mathbf{x}_e$, add it to the simplex and return to point **1**. If not, add $\mathbf{x}_r$ to the simplex and return to point **1**.

4: contraction
If $f(\mathbf{x}_n) \leq f(\mathbf{x}_r) < f(\mathbf{x}_{k+1})$, then perform an outside contraction (Figure 5-1(c)).

$$\mathbf{x}_c = \bar{\mathbf{x}} + \psi(\mathbf{x}_r - \bar{\mathbf{x}}) = \bar{\mathbf{x}} + \psi\rho(\bar{\mathbf{x}} - \mathbf{x}_{k+1}) = (1 + \psi\rho)\bar{\mathbf{x}} - \psi\rho\mathbf{x}_{k+1} \tag{5-7}$$

Obtain and evaluate $f(\mathbf{x}_c)$. If $f(\mathbf{x}_c) < f(\mathbf{x}_r)$, add $\mathbf{x}_c$ to the simplex and go to point **1**, otherwise go to point **5** and perform a shrink.

If $f(\mathbf{x}_r) \geq f(\mathbf{x}_{k+1})$, then perform an inside contraction (Figure 5-1(d)).

$$\mathbf{x}_{cc} = \bar{\mathbf{x}} - \psi(\bar{\mathbf{x}} - \mathbf{x}_{k+1}) = (1 - \psi)\bar{\mathbf{x}} + \psi\mathbf{x}_{k+1} \tag{5-8}$$

Obtain and evaluate $f(\mathbf{x}_{cc})$. If $f(\mathbf{x}_{cc}) < f(\mathbf{x}_r)$, add x_{cc} to the simplex and go to point **1**, otherwise go to point **5** and perform a shrink.

5: shrink
Shrink the simplex so that

$$\mathbf{v}_i = \mathbf{x}_1 + \sigma(\mathbf{x}_i - \mathbf{x}_1), \quad \text{for i = 2:k+1} \tag{5-9}$$

This operation is shown in Figure 5-1(e). The new simplex consists out of vertices $\mathbf{x}_1, \mathbf{v}_2, \ldots, \mathbf{v}_{k+1}$. Return to point **1**.

These operations led to the flowchart in Figure 5-2.

5-3 Modal optimization

As mentioned in [5], the use of modal optimization can speed-up the convergence.
Modal optimization gives gives the possibility to limit the number of parameters optimized, by limiting the number of modes to be optimized.
One other big advantage of modal optimization is that some types of aberration present in the AO setup, are directly related to the shape of certain modes. So is misalignment of the pinhole directly related to tip, tilt and defocus modes and is the initial aberration of the mirror spherical [6]. Almost all new papers published on WFSless AO make use of orthogonal modes[19][20][21][22]. Some of these methods cannot be tested, since they require the use of a camera [19][21]. The center of mass optimization described by Booth [22], offers the possibility of quick optimization, finding the optimum with $m + 1$ function evaluations, with m the number of Zernike modes evaluated. However this method only works for aberrations with a maximum amplitude of 1 rad. In this thesis aberrations have larger amplitudes, making it impossible to use this method. One other comment that needs to be made, is that near the optimum function values are close to one another and the influence of noise is relative large, corrupting found optima.
In the next Subsections three modal OA will be explained that are able to compensate for larger amplitudes.

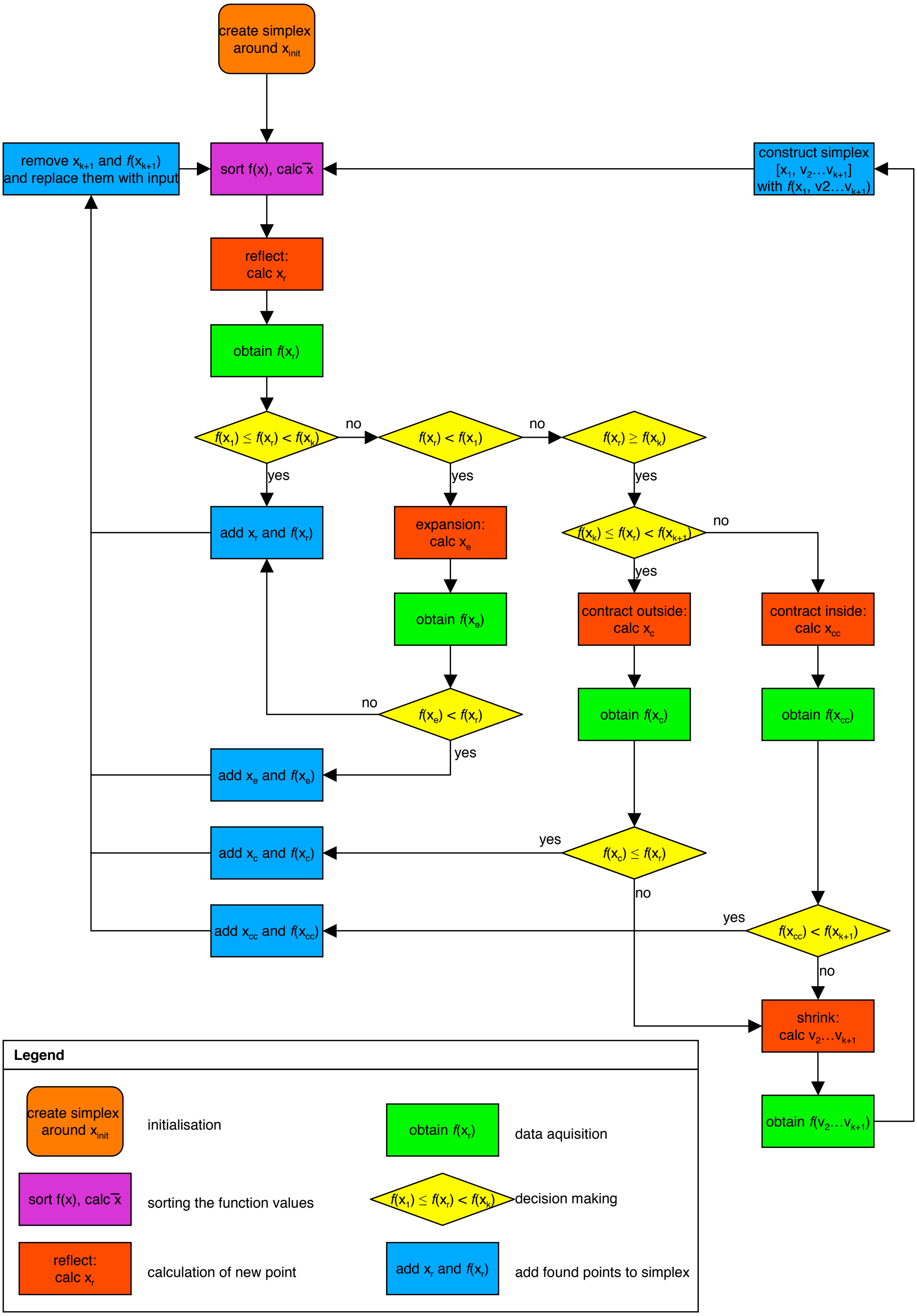

Figure 5-2: Flowchart describing the Nelder-Mead simplex.

5-3-1 Nelder Mead Simplex

De Boer [4] only tested the Nelder-Mead (NM) simplex while optimizing the voltages of the DM. In his recommendations he advised to adapt the NM simplex for the use of modal optimization. This can be done without mayor difficulties and changes in the algorithm. The algorithm is exactly the same as in Section 5-2-1, only the constraints are different and the output is scaled to correspond with the coefficients and initial values of the Zernike modes.

5-3-2 Zernike mode line search

The Zernike mode line search (LS) was already tested by de Boer [4] to maximize light intensity and was the algorithm that led to the highest intensity results tested in his WFSless AO setup. This algorithm m Zernike modes were optimized as an $m \times 1$-dimension problem. The algorithm has also been tested by Grisan [21], only was this test a simulation in which a camera was simulated. After one coefficient has been optimized, all previous modes will be optimized again, making his optimization process m-dimensional. This thesis repeats the LS algorithm test of the de Boer, since it gave the highest light intensity results. And to investigate the effect of reducing the m-dimensional problem of the NM simplex to an $m \times 1$-dimensional problem. The algorithm creates a cost function over a p number of points of a Zernike mode coefficient, stored in matrix $\mathbf{r}$, and maximizing by picking the value of the coefficient where the cost function has its maximum.

$$\beta^*_{mode} = \arg\max_{\mathbf{r}} f(\mathbf{r}, \beta_{opt}, \beta_{guess}, \phi_{ab}) \tag{5-10}$$

where β_{mode} is coefficient of the Zernike mode being optimized and contains the found optimum. $\mathbf{r}$ is the range over which is searched for the optimum. In general

$$\mathbf{r} = (-\text{bias} : \frac{2 \cdot \text{bias}}{p-1} : \text{bias}) + \beta(i)_{guess} \tag{5-11}$$

where the bias is depended on the mode being optimized, since not all modes require an evenly large range. $\beta(i)_{guess}$ is the guess for the optimum of a certain coefficient of Zernike mode. β_{opt} is an array, containing the optimal coefficients for the modes already optimized. β_{guess} contains initial estimations of the upcoming modes. The shape of the mirror during the optimization at the time that mode m_n is evaluated at point p_i of the range, can be described as:

$$h(x,y) = \mathbf{r}(p_i) Z_{m_n}(x,y) + \sum_{n=1}^{m_n-1} \beta_{opt,i} Z_i(x,y) + \sum_{n=m_n+1}^{m} \beta_{guess,i} Z_i(x,y) \tag{5-12}$$

The optimization process of one mode is shown in Figure 5-4. The number of iterations for the described method is fixed. The optimization method quits after $p \cdot m + 1$ time samples. As p increases the grid will become finer and the optimum found will be more precise, however, this also increases the time needed to find an optimum. This method can be considered as a predecessor for the quadratic optimization (QO) method, discussed in the next Section.

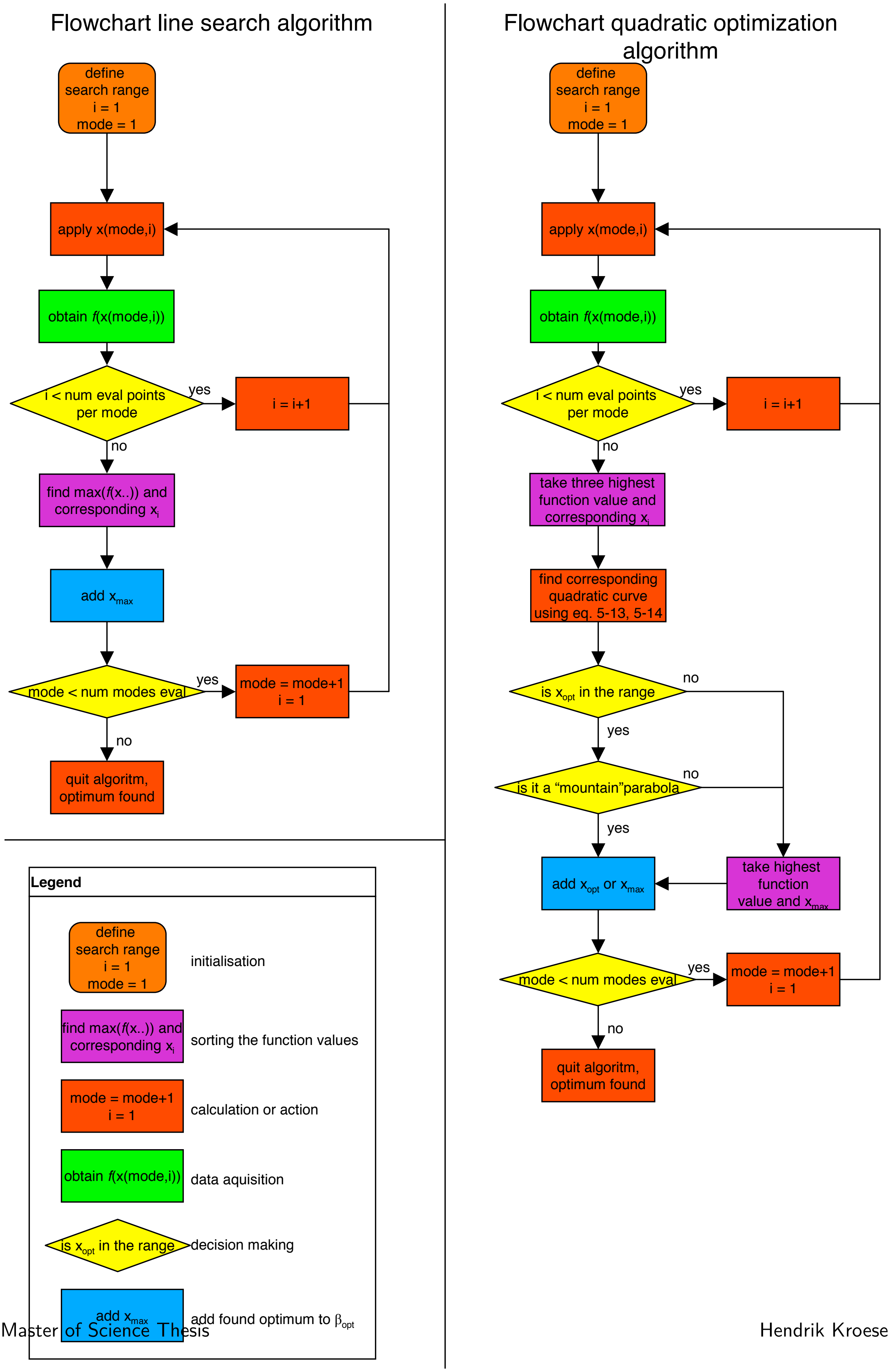

Figure 5-3: Left: flowchart describing line search algorithm. Right: flowchart describing quadratic optimization algorithm.

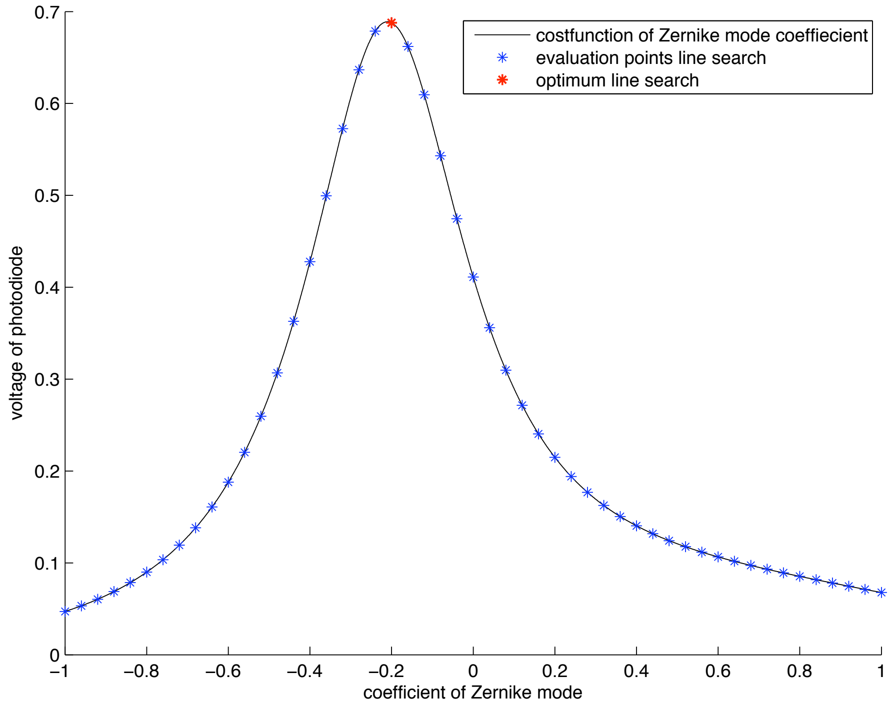

Figure 5-4: Example showing the line search method finding its optimum.

5-3-3 Quadratic optimization

Debarré [20] showed that the cost function of individual Lukosz modes in proximity of the optimum shows quadratic behavior, making it possible to find the optimum with only three function evaluations. However if the optimum is located outside these points, the cost function will not resemble a parabola any more. In order to find an optimum for larger aberration, the method needs to be extended. One possibility how this can be achieved is by combining the LS method and the QO.
Debarré used only three functions evaluations and a camera and could only compensate for small aberrations. The use of the camera resulted in no compensation for tip and tilt, since this the x,y offset can already be observed by the camera. In this thesis a pinhole is used and an attempt is done to compensate for larger disturbances.

To increase the chances to find the optimum of a mode, the number of p points per mode is increased. So instead of three points, seven points are evaluated, this is exactly the same as the Zernike mode LS, except that the number of points, p, is reduced. The shape of the mirror at a certain time is as in equation 5-12. Difference is in the way the maximum is calculated. Where as with the Zernike mode LS the maximum over range $\mathbf{r}$ is taken; in QO, the three highest function points $\mathbf{f}_{max} \in \mathbb{R}^3$ are taken and the corresponding coefficients are saved in array $\mathbf{r}_{max} \in \mathbb{R}^{3\times m}$.

$$\mathbf{f}_{max} = \arg\operatorname{sort} f(\mathbf{r}, \beta_{opt}, \beta_{guess}, \phi_{ab}) \tag{5-13}$$

It is assumed that these functions are located around the optimum where quadratic behavior is present.
Now the parameters that will create quadratic function $\mathbf{f}_{max} = a \cdot \mathbf{r}_{max}^2 + b \cdot \mathbf{r}_{max} + c$ can be calculated.

$$\begin{bmatrix} a \\ b \\ c \end{bmatrix} = \begin{bmatrix} \mathbf{r}_{max}(1)^2 & \mathbf{r}_{max}(1) & 1 \\ \mathbf{r}_{max}(2)^2 & \mathbf{r}_{max}(2) & 1 \\ \mathbf{r}_{max}(3)^2 & \mathbf{r}_{max}(3) & 1 \end{bmatrix}^{-1} \cdot \begin{bmatrix} \mathbf{f}_{max}(1) \\ \mathbf{f}_{max}(2) \\ \mathbf{f}_{max}(3) \end{bmatrix} \tag{5-14}$$

The optimum can be found by taking the derivative of the function and putting it equal to zero. This leads to

$$\beta^*_{mode} = \frac{-b}{2 \cdot a} \tag{5-15}$$

It can happen under certain conditions that the optimum that is calculated, is not a maximum, but a minimum. In this situation the value of a is positive. If this situation occurs, the location of the highest function values will be elected to be the coefficient of the specific Zernike mode.

$$\beta^*_{mode} = \arg\max_{\mathbf{r}} f(\mathbf{r}, \beta_{opt}, \beta_{guess}, \phi_{ab}) \tag{5-16}$$

However, it can also happen that the optimum is outside of the search range $\mathbf{r}$. If $\beta^*_{mode} > \max(\mathbf{r})$ or $\beta^*_{mode} < \min(\mathbf{r})$, the location where the highest function value was found will be taken as optimum. In this case, equation 5-16 is again used.

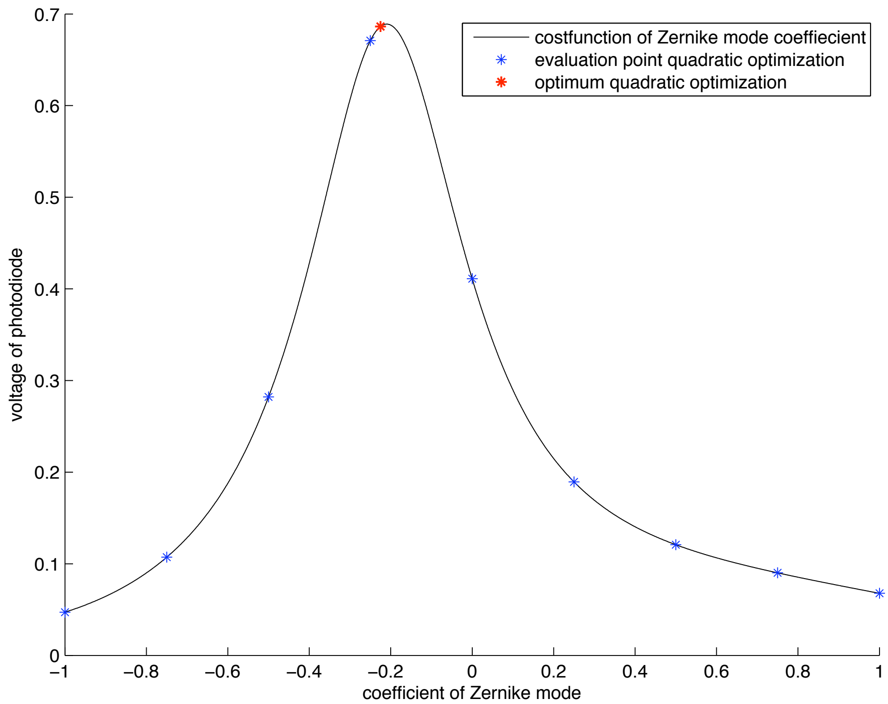

Figure 5-5: Example showing the quadratic optimization method finding its optimum.

5-4 Conclusion

All controllers mentioned in this Chapter were tested on the AO setup. The tests were performed with and without hysteresis compensation.

Chapter 6

Experimental Results

6-1 Introduction

In this Chapter the following control algorithms will be tested: the Nelder-Mead (NM) simplex where the driving voltages are controlled, the NM simplex where the shape of the mirror is controlled with 14 Zernike modes, a line search (LS) over the 14 Zernike modes and a quadratic optimization (QO) over 14 Zernike modes. These tests are conducted with and without hysteresis compensation (HC) to discover, whether this extra compensation improves the convergence speed and/or a higher final light intensity value is obtained. The setup, which is used to perform the test, is described in detail in Section 2-2. Schematics of the setup where the OAs and the hysteresis compensator are experimentally tested are shown in Figure 6-1, the corresponding block diagram is given in Figure 6-2. In the next Section the disturbance applied to the setup, which negative effects on the light intensity the OA will try to minimize, is discussed.

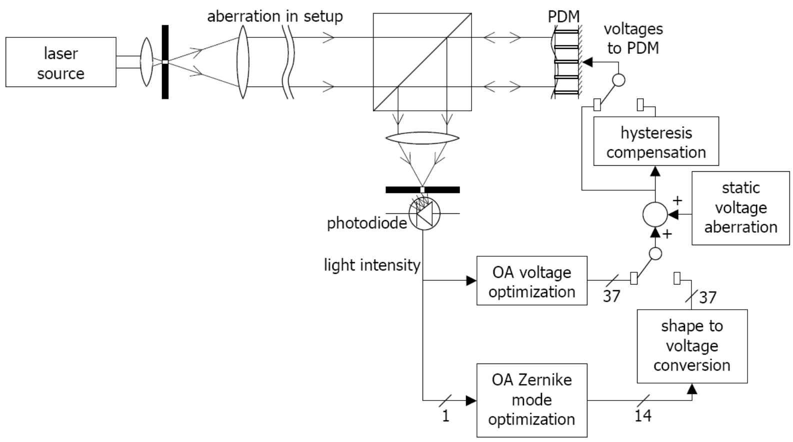

Figure 6-1: Schematics of the experimental setup used to obtain the experimental results.

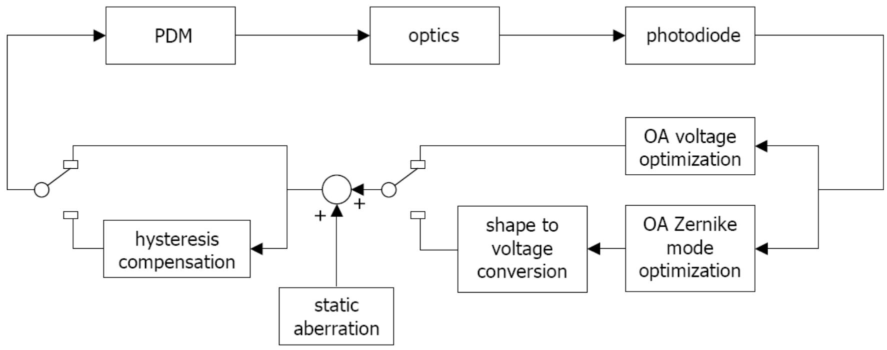

Figure 6-2: Block diagram of the experimental setup, as shown in Figure 6-1.

6-2 Aberration

The disturbance to be compensated for, is partially present in the system due to misalignments of optical components. However extra static aberration is introduced by applying offset voltages to the DM. This aberration, introduced by voltage offsets, is generated as a number of random Zernike mode coefficients.

$$\alpha_{norm,generate} = 2 \cdot \mathrm{rand}(m,1) - 1 \tag{6-1}$$

With m the number of Zernike modes being optimized. It was decided to take mode 1-14, omitting piston mode 0. Now the corresponding voltages can be found with help of conversion matrix M_{mirror} (equation 3-17).

$$\begin{aligned} \mathbf{h}_{\text{norm,offset}} &= \textstyle\sum_{i=1}^{m} \alpha_{norm,generate} \cdot Z_i = \mathbf{M}_{mirror} \cdot \mathbf{v}_{\text{norm,offset}} \quad \rightarrow \\ \mathbf{v}_{\text{norm,offset}} &= \mathbf{M}_{mirror} \backslash (\textstyle\sum_{i=1}^{m} \alpha_{norm,generate} \cdot Z_i) \end{aligned} \tag{6-2}$$

By applying offset voltages to the mirror, part of the voltage range over which optimization can take place is occupied. This extra offset increases the possibility of saturation of the actuators during optimization. If actuators are saturated, the relation between the voltages or shapes and the corresponding intensity measurement is lost. Light intensity optimization tests were performed, where the minimum and maximum where observed, to see how the voltages needed to be scaled, so saturation would not occur in all tested algorithms. This demand was fulfilled if the minimum voltage of $\mathbf{v}_{\text{offset}}$ is 75 volts and the maximum 125 volts.

$$\mathbf{v}_{\text{offset}} = \frac{\mathbf{v}_{\text{norm,offset}} - \min(\mathbf{v}_{\text{norm,offset}})}{(\max(\mathbf{v}_{\text{norm,offset}}) - \min(\mathbf{v}_{\text{norm,offset}}))} \cdot (125 - 75) + 75 \tag{6-3}$$

During testing 100 tests are performed. The aberration in these tests consisted out of 10 aberration sets, obtained as described above. Each aberration set was optimized 10 times.

6-3 Analysis

As mentioned in Section 2-4 the performance criteria consist out of the final light intensity value of the photodiode which the algorithm can achieve, but also the convergence time. For the Zernike mode LS and QO, this time is fixed; it is the number m of modes evaluated times the number of tests p per coefficient. The NM simplex does not stop, but will constantly search for a higher function value. However, at a certain point, the points in the simplex are so close together that it almost does not influence the photodiode voltage any more. One other thing to be taken into account while evaluating the convergence speed, is the fact that the optimization of the NM simplex is not smooth. A good or bad point in the simplex can cause a large spike in the intensity measurements. An example of this is given in Figure 6-3. The blue line is optimization

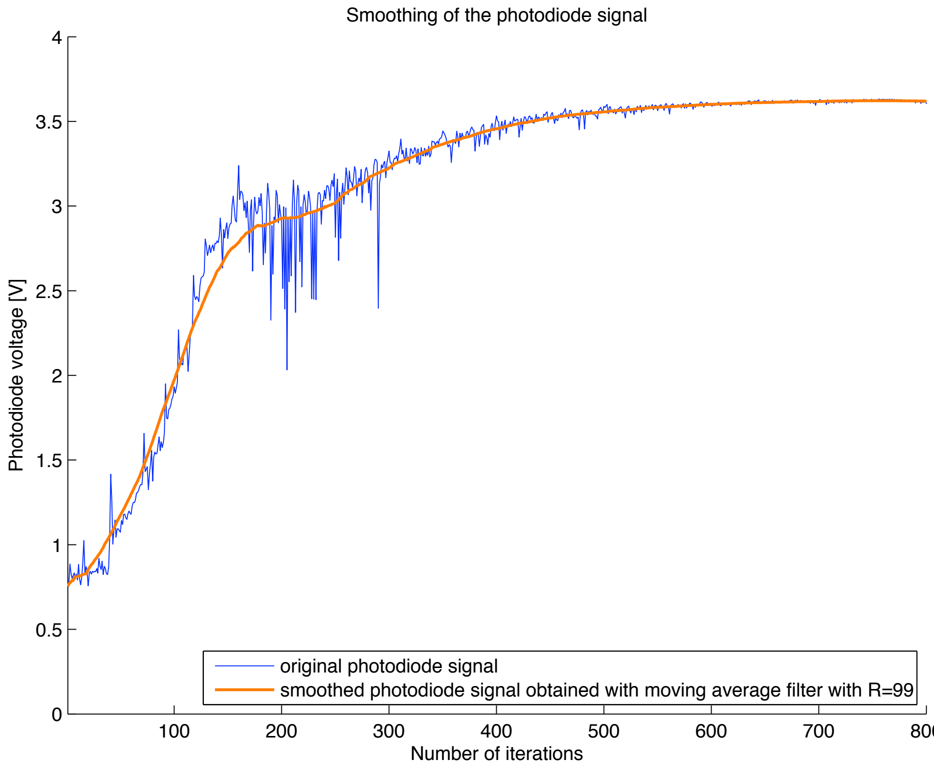

Figure 6-3: Effect of applying a moving average filter to an light intensity optimization performed by the Nelder-Mead simplex.

performed with the NM simplex. For this line, it is difficult to say when it gets within 95% of its final light intensity value. To be able to do so, a smoother line is needed. That is why the photodiode signal will be filtered through a moving average filter with smoothing factor $R = 99$. The filtered signal is calculated as follows:

$$x_{smooth}(i) = \begin{cases} \frac{\sum_{1}^{(i-1)\cdot 2+1} x(i)}{(i-1)\cdot 2+1} & \text{for } \; i < (R-1)/2 \\ \\ \frac{\sum_{i\cdot 2-L}^{L}}{(L-i)\cdot 2+1} & \text{for } i > L-(R-1)/2 \\ \\ \frac{\sum_{i-(R-1)/2}^{i+(R-1)/2} x(i)}{R} & \text{for all other } \; i \end{cases} \tag{6-4}$$

where L is the length of the data array x. The result of using formula 6-4 to smooth the photodiode signal, is the orange line in Figure 6-3.

6-4 Results

6-4-1 Nelder-Mead simplex, voltage optimization

The NM simplex method was used in the past and gave relatively fast and quite reliable convergence in a way that the algorithm would stop optimizing, before the optimum was found.[5] This was motivation to take this algorithm as reference algorithm.

In Figure 6-4 the final light intensity values are shown. It is clearly visible that the use of hysteresis compensation increases the performance of the NM algorithm. The graph gives insight into how this is achieved. First: the number of optimizations that fail is reduced; secondly: the optimization leads also to higher values.
This result is not surprising, taken into account that the NM algorithm is used. In this algorithm photodiode values are linked to a simplex. If hysteresis is present, the exact heights of the actuators corresponding to this simplex will most likely not be reproduced, if the values of the simplex is again put on the mirror. In short: the shapes stored in the simplex are not at the same simplex location when applied again, so the data is less reliable. Due to the properties of hysteresis, this effect will be larger for larger differences in shape.

The other property on which the performance of the algorithm will be judged is the time needed to get close to the final light intensity value. In Figure 6-5, the average over all 100 smoothed curves is taken and compared. In percentage the convergence of the NM simplex with HC is slower in time (the percentages lay more to the right on the horizontal time axis compared to the situation without HC). However, this comparison does not show everything, since the final light intensity achieved by the algorithm without hysteresis compensation is lower. In fact, in the situation without hysteresis compensation the algorithm hits 95% of its end value in about 425 iterations, while with HC, the system just "only" past 93%. But at this 93% the output of the photodiode is higher than in the situation without HC. Thus the situation with HC performs better.

6-4-2 Nelder-Mead simplex, Zernike mode optimization

De Boer [4] recommended to adapt the NM simplex for optimizing Zernike modes. This adjustment was done, however it did not lead to a drastic improvement of the light intensity, as can be seen in Figure 6-6. With an average photo diode voltage of 3.506 Volts for the situation without hysteresis compensation and 3.488 Volts for the situation with hysteresis compensation, the result is slightly better than 3.487 Volts.

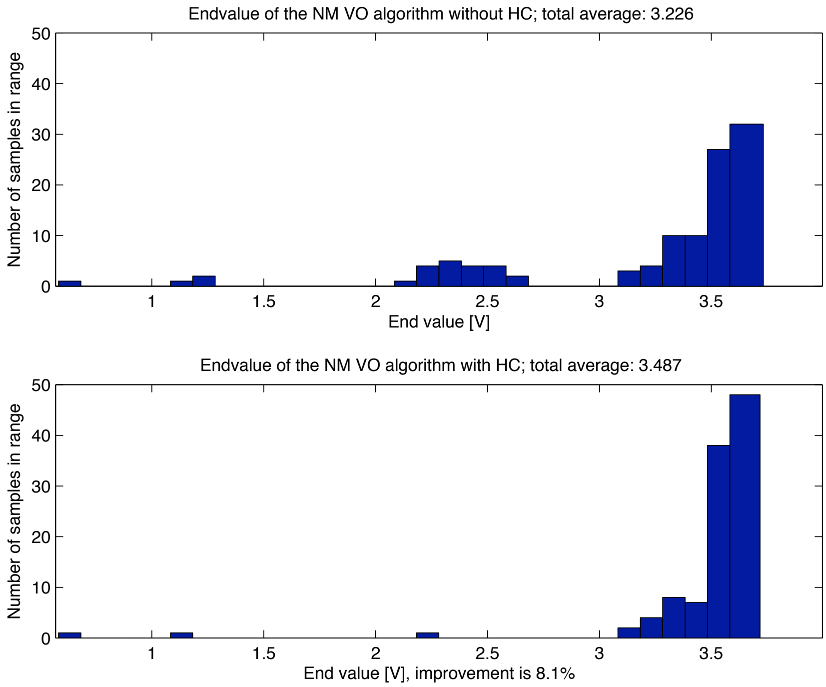

Figure 6-4: Histogram with the final light intensity value of voltage optimization, using the Nelder-Mead simplex. Hysteresis compensation leads to less premature failure and a higher average light intensity.

Something else what can be observed is that the amount of failed optimizations is drastically reduced. While with voltage optimization (especially when hysteresis was not compensated) it sometimes happened that the voltage did not even reach 3.2 Volts, it totally did not happen when the shape was optimized. A remarkable thing is that the HC did not lead to better results. The results are slightly worse (-0.5%), which can be due to noise in the setup and environment. In general, it can be said that the NM simplex in combination with shape optimization delivers more consistent final light intensity values, where as the benefit of HC is not noticeable.

As said, in light intensity, the Zernike mode optimization did not achieve much better results than voltage optimization together with HC, however, the convergence speed also needs to be evaluated. Here a huge difference emerges if Figures 6-5 and 6-7 are compared. For instance, if is investigated when on average the photo diode value passes 3 Volts, in case of voltage optimization without hysteresis compensation this is around 385 iterations, with hysteresis compensation this value is 315. For shape optimization, with and without HC, it takes 130 steps! This is an average reduction of 59-66%!

6-4-3 Zernike mode line search

In the Zernike mode LS algorithm, it was tried to reduce the problem from a m dimensional problem to a $m \times 1$ dimensional problem, where m is the number of Zernike

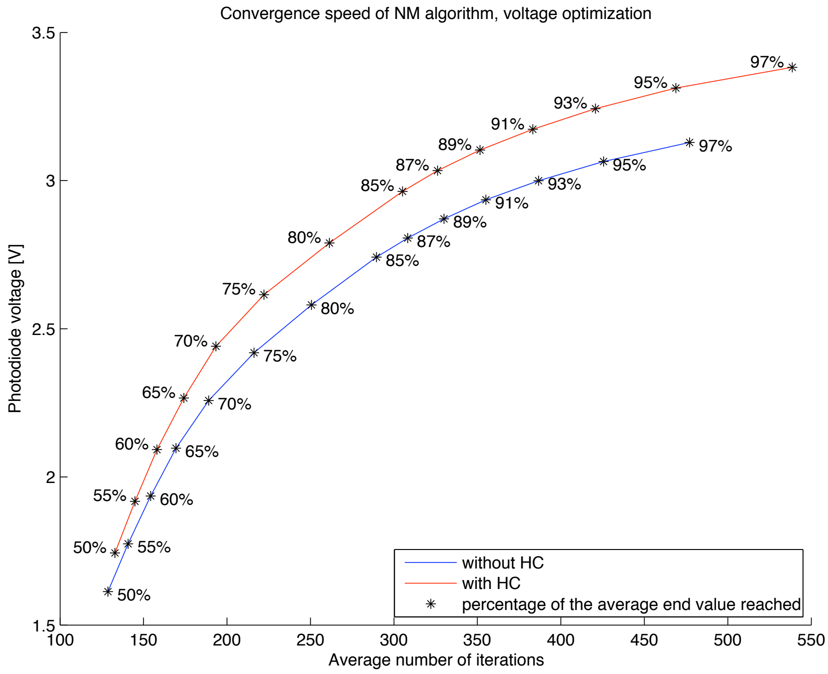

Figure 6-5: Learning curve of the WFSless AO setup with the Nelder-Mead voltage optimization, with and without hysteresis compensation.

modes being evaluated. This was partially successful, the light intensity did not reach the same level as the NM simplex algorithms. The photodiode produced an average voltage of 3.271 V for the situation without HC 3.353 V and with hysteresis compensation. For the case without HC this is higher than the NM simplex in VO with hysteresis compensation. It is likely this is only due to the amount of failed optimizations while using the NM simplex. If the cases with HC are used, a clear difference becomes visible. The NM simplex reaches a higher light intensity, this is not strange, since the LS algorithm only solves a 14×1-dimensional problem and the NM simplex in VO solves a 37-dimensional problem. However, the LS always gets close to the optimum and, in contrary to the NM in VO, never fails half way.

Last thing that needs to be compared, is the effect of hysteresis compensation on the light intensity. As can be seen in Figure 6-8, the LS with HC performs better than without. A possible explanation can be found in Section 4-6, where the cost functions from Zernike modes were evaluated. It became visible that due to hysteresis the cost function consists out of 2 curves, making an optimum found in LS, harder to be found again. The effect of this can be seen in Figure 6-9.

It is not possible to speak about convergence speed with the line search algorithm. It has a fixed amount of steps. However Figure 6-9 shows how the algorithm converges towards the optimum. The asterisks in the graph are located at the initial guess of the coefficient of that specific Zernike mode. As result, at the place of an asterisk, it can

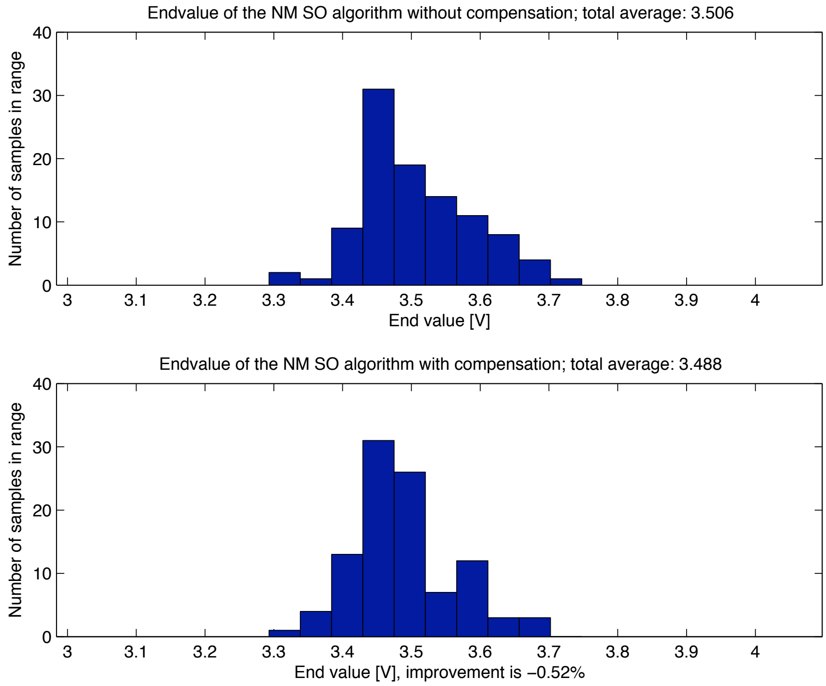

Figure 6-6: Histogram showing the final light intensity values of Zernike mode optimization, using the Nelder-Mead simplex. Hysteresis compensation does not lead to better results.

be visible what the optimization algorithm has been achieved in the previous mode. In the ideal case, the dashed line through the asterisks will always be ascending (this implies that optimization of a mode will never lead to a lower light intensity). When HC is activated, this is the case. In Figure 6-9 it can be seen that without HC the line also goes down. This means that while optimizing the next mode, the optimal shape found in the previous coefficient optimization cannot be applied to the mirror again, most likely due to hysteresis.

6-4-4 Zernike mode quadratic optimization

In Section 5-3-3, QO is introduced to reduce the number of points evaluated per Zernike mode coefficient. The location of the maximum can now be found by fitting a quadratic curve through the highest points and finding the maximum of the parabola. This was tested in the setup. As effect the number of evaluation points per coefficient was reduced from 51 to 7, while the algorithm was still able to get close to the optimum. However the final light intensity is slightly lower than those obtained with the Zernike mode LS algorithm. This is not surprising, since the area around the optimum is approximated with a parabola, although in reality it is not sure whether the elected points for constructing a parabola are close enough to this optimum. The option of noise the corrupting reconstruction of the quadratic function and the corresponding maximum is not even mentioned.

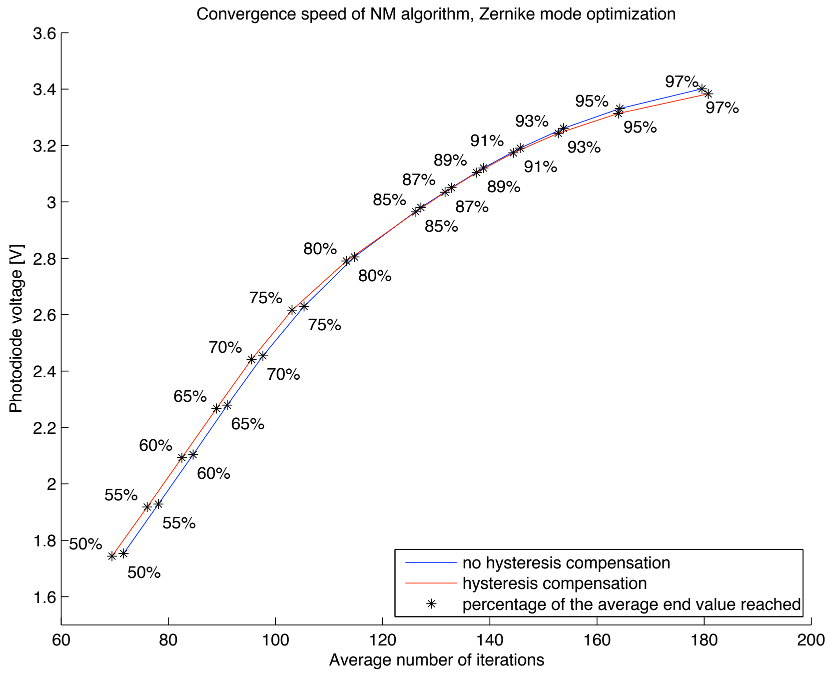

Figure 6-7: Learning curve of the WFSless AO setup with the Nelder-Mead Zernike mode optimization, with and without hysteresis compensation.

Like the LS algorithm, it happens that after optimization of a Zernike mode coefficient the light intensity is lower than before. For the LS algorithm, this was explained by the presence of hysteresis. However, in case of HC in combination with QO, this is still the case. Of course it is possible that this is partially due to hysteresis still present in the system after compensation, but the most plausible reason for this effect is that the QO for that specific mode was not able to find the right optimum, and is moving away from the optimum. In general, it can be said that QO is able to get close to the highest light intensity fast (in $7 \cdot 14 = 98$ iterations), but due to the fact it assumes the cost function to be quadratic and because it is optimizing an $m \times 1$-dimensional problem (instead of an m-dimensional problem), it is not always able to reach the highest light intensity.

Table 6-1: Summary of experimental results

	Light intensity [V]		Average number of steps to reach 3V	
	no HC	with HC	no HC	with HC
Nelder-Mead voltage optimization	3.226	3.487	387	326
Nelder-Mead Zernike mode optimization	3.506	3.488	129	129
Zernike mode line search	3.271	3.353	434 (after ZM8)	230 (after ZM4)
Zernike mode quadratic optimization	3.248	3.327	60 (after ZM8)	60 (after ZM8)

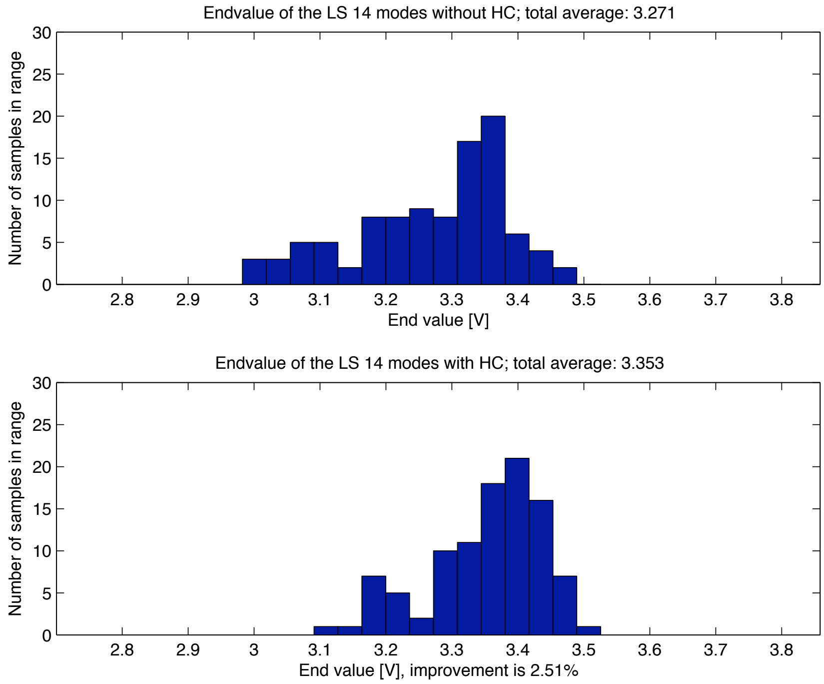

Figure 6-8: Histogram showing the final light intensity values of Zernike mode optimization, using the line search algorithm.

6-5 Conclusion

If voltage optimization is compared to Zernike mode optimization, two things are noticed. First with Zernike mode optimization, the time needed for optimization can be reduced. Secondly: if the NM simplex is compared in voltage optimization and in Zernike mode optimization, the amount of failures while optimizing is reduced.

When the Zernike mode OAs are compared, the LS is the slowest algorithm, however this is partially depended on the number of points evaluated per coefficient. On average the NM simplex is able to reach a light intensity of 3 Volts in 129 steps, where the QO finishes in 60 steps, but is not able to reach the same light intensity. On the contrary, the voltage measured by the photodiode after 60 steps with the NM is less than 1.8 Volt.

The NM optimizations lead to the highest light intensity, which can most likely be attributed by the fact they solve a multi-dimensional problem instead of a $m \times 1$ dimensional problem.

HC leads in most of the cases to a better result. It improves the ability to reproduce a found optimum shape. In case of NM VO it also implies that this ability reduces the possibility of failure. However, for the NM in Zernike mode optimization, no benefit of HC was found.

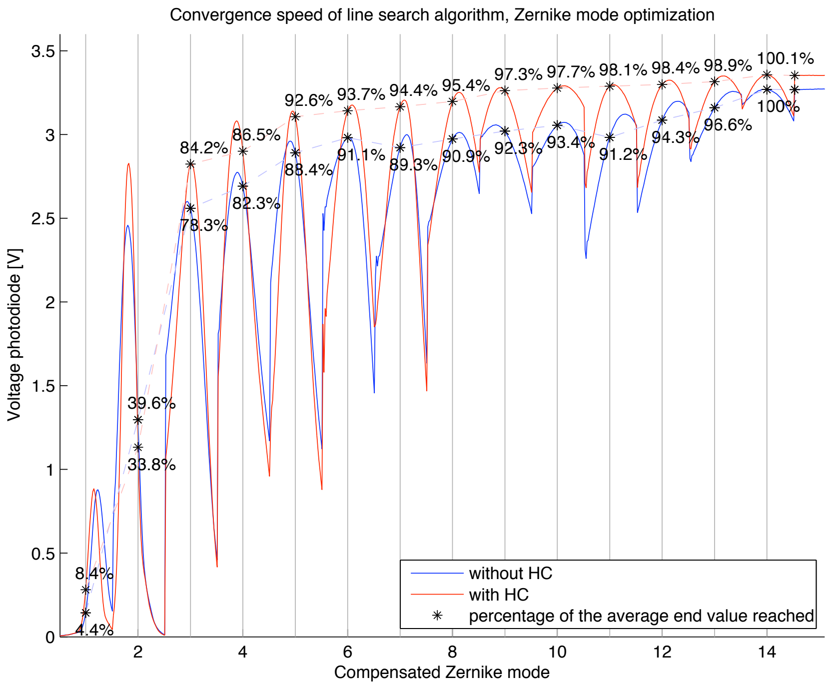

Figure 6-9: Average light intensity, as Zernike mode coefficients are optimized with the line search algorithm. With hysteresis compensation the photodiode values passed 3 Volts after Zernike mode 4. Without hysteresis compensation this only happens after optimization of Zernike mode 8.

For future research, trying to improve WFSless AO, it can be advised to investigate the possibility of a hybrid controller: the quadratic optimization to get close to the optimum and from there use a controller that is better able to find this optimum, like the NM simplex (whether this is for optimizing voltages or Zernike modes).

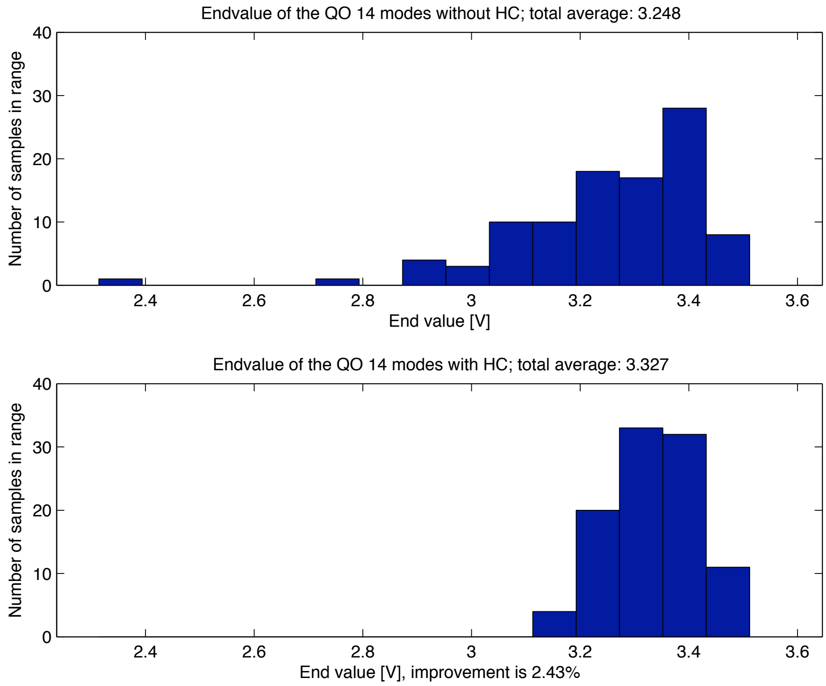

Figure 6-10: Histogram showing the final light intensity values of Zernike mode optimization, using the quadratic optimization algorithm.

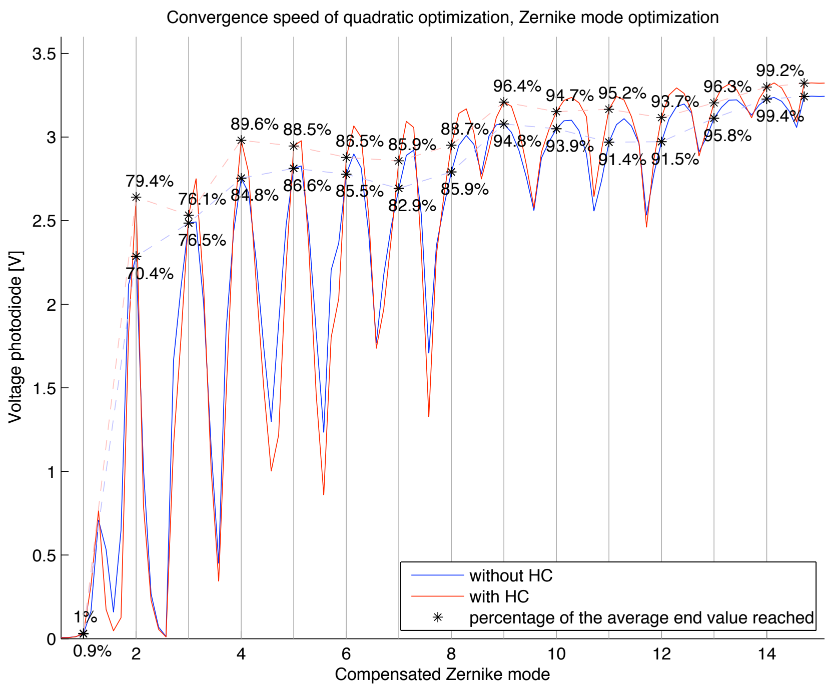

Figure 6-11: Average light intensity, as Zernike mode coefficients are optimized with the quadratic optimization algorithm. After Zernike mode 8 is optimized, the values of photodiode are above 3 Volts, with and without HC.

Chapter 7

Conclusion and Recommendations

This chapter contains the conclusions and recommendations drawn from the research and experiments conducted in this report.

7-1 Conclusions

The conclusions are divided in two parts. The first part handles conclusions that are related to hysteresis compensation (HC). The second part considers conclusions that were derived from the experimental results.

7-1-1 Conclusions concerning hysteresis compensation

- It is possible to identify hysteresis curves of a piezo deformable mirror with help of the Foucault knife edge test. With the hysteresis curves it is possible to create an inverse hysteresis model, which can reduce the effects of hysteresis, present in the piezo deformable mirror.
- For the used 37-channel piezo deformable mirror, inverse hysteresis models, identified with an actuator with suitable curves, could also be used to reduce the effects of hysteresis for other actuators.
- The Coleman-Hodgdon equations can be adjusted such that the inverse hysteresis curve can immediately be calculated. By using information about local minima and maxima the number of variables could be reduced from 6 to 2. This gave the possibility to make one of the parameters dependent on other variables, so hysteresis curves can be approximated better.
- Without HC, the cost function of Zernike modes has in general two curves: each for increasing and decreasing values of the Zernike coefficient. With HC in 8 out

of the 12 examined modes, the curves merged together and therefore reduced the uncertainty in the cost functions.

7-1-2 Conclusions concerning the experimental results

- The Nelder-Mead simplex was able to achieve the highest light intensity of all algorithms.
- If the NM simplex optimizes Zernike 1-14, instead of the 37 driving voltages, the algorithm needs 59-66% less steps to reach 95% of the average final light intensity.
- In order to quickly convergence to the location of the maximum light intensity, it is possible to perform $m \times 1$ dimensional quadratic optimization problem, which finds approximate solution for the Zernike mode coefficients. The quadratic optimization needs only 60 steps to reach 3 Volts (about 80% of the highest light intensity), whereas the Nelder-Mead simplex in Zernike mode optimization needs 129 steps.
- In case of the NM voltage optimization, the Zernike mode line search and the Zernike mode quadratic optimization leads on average to a higher light intensity. In case of the NM voltage optimization, HC reduces the possibility of premature failure.

7-2 Recommendations

The recommendations will be split-up in three parts. First part will handle HC, the second will consider recommendations which might improve the light intensity optimization process, last will be recommendations for improvement of the optical setup.

7-2-1 Hysteresis compensation recommendations

- The parameters of the inverse C-H eq. are identified based on a limited number of hysteresis curves. If more curves are known, it might be possible to give even better approximation of the curves. This might lead to better modeling of parameter D. Now an exponential function is used, but there might be better alternatives.
- A big contribution to WFSless AO would be reconstruction of the hysteresis curves with help of the lens/pinhole/photodiode, instead of the Foucault knife edge test, making WFSless setups even simpler. Tests conducted in this project show the potential, however, no identification was done using this method. If the desired curves do not emerge, a knife can be placed in front of the pinhole to tune the signal.

7-2-2 Optimization algorithm recommendations

- Create a hybrid controller, which uses the Zernike mode quadratic optimization to quickly approach the optimum and after that switch to the Nelder-Mead simplex for finding the highest possible intensity.
- Investigate which Zernike modes are most present for common WFSless aberrations and determine in which sequence the coefficients of the Zernike modes can be optimized best. If some modes are hardly present, it may be wise to skip this optimization, making the quadratic optimization faster and leaving these modes to be compensated by the Nelder-Mead simplex.
- Implement an x-y position measurement device. With this device it should be possible to compensate for even larger disturbances of tip and tilt. Once these modes are compensated, the WFSless algorithms investigated in this thesis can take over the optimization.

7-2-3 Setup recommendations

- Shield the setup from external light influences. Best way to put the setup at a location where sunlight cannot come. In the current setup the sensor had to be totally capsulated, making it more difficult to adjust the setup when needed.
- Reduce the influence of vibrations. This can be achieved by multiple ways. One possibility is to hang the current setup to the ceiling, like a pendulum. The larger the length of the ropes, the lower the influence of vibrations in the building. This method is for instance used for electron microscopes. One other possibility is to replace the current breadboard by a heavier one and mount the breadboard on legs with dampers. In this case, it will be easier to implement the WFSless components in other AO setup, present at DCSC.
- Integration of the WFSless setup in the other setup would also have one other benefit. It would give the possibility to use the Shack-Hartmann sensor to observe the wavefront. It gives insight into what kind of aberration is still left in the system, after the light intensity is optimized. Also it would give insight into which modes are dominant in the aberration, leading to better strategies to reduce disturbance in WFSless setups.

Appendix A

Zernike modes

As mentioned in subsection 3-2-2 is it possible to describe the wavefront as a summation of orthogonal modes, each shape multiplied with its own coefficient. One of the most used ways to describe the shape is with help of the Zernike polynomials. The height wavefront at a certain point (ρ, θ) can be described as

$$h(\rho, \theta) = \sum_{i=0}^{\infty} a_i Z_i(\rho, \theta) \tag{A-1}$$

$Z_i(\rho, \theta)$ is here the height corresponding to the i^{th} Zernike mode at location (ρ, θ). a_i is the Zernike coefficient of the i^{th} mode.
The Zernike polynomials can be calculated as follows [4]:

$$Z_i(\rho, \theta) = \begin{cases} R_r^o(\rho)\cos(o\theta) & , \ o > 0 \\ R_r^o(\rho)\sin(o\theta) & , \ o < 0 \\ R_r^o(\rho)\cos & , \ o = 0 \end{cases} \quad \text{(A-2)}$$

with

$$R_r^o(\rho) = \sum_{s=0}^{\frac{r-o}{2}} \frac{(-1)^s (r-s)!}{s![(r+o)/2+s]![(r-o)/2-s]!} \rho^{r-2s} \tag{A-3}$$

For optimizations the Zernike mode 1-14 were optimized. Mode 0, piston, was not optimized, since this mode does not influence the light intensity. In table A-1, conversion from Zernike mode i to radial frequency r and order o.

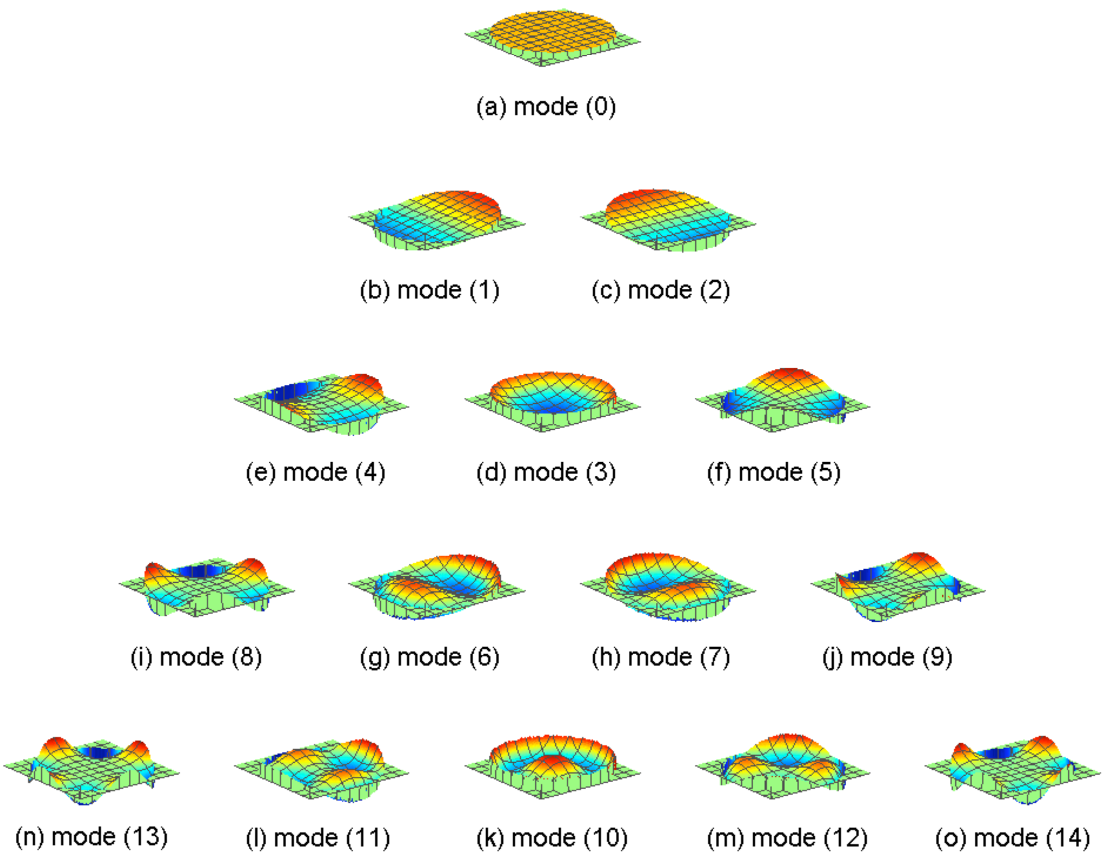

Figure A-1: Visualization of the first 15 Zernike modes, numbered as in the optimization algorithms.

Table A-1: Conversion table from radial frequency r and order o to Zernike mode i.

r \o	-4	-3	-2	-1	0	1	2	3	4
0					i=0				
1				i=1		i=2			
2			i=4		i=3		i=5		
3		i=8		i=6		i=7		i=9	
4	i=13		i=11		i=10		i=12		i=14

Appendix B

Optics Setup Component List

Table B-1: List of optical components used in the AO setup

component	manufacturer	number	details
1 optical breadboard	Eksma	1HB06-09-07	60 x 90 cm
1 laser + power supply	Melles Griot	25 LHP 213	HeNe/1mW
1 spatial filter	Eksma		
1 microscope objective	Eksma	OM-27	$f = 8.4$ mm
2 precision pinholes	Eksma	990-0010	$d = 10$ μm
	Edmunds	NT56-282	$d = 50$ μm
2 lenses	Edmunds	NT45-154	$f = 250$ mm
	Edmunds	NT45-287	$f = 400$ mm
2 beam splitter cubes	Edmunds	NT32-505	25x25x25 mm
	Edmunds	NT32-506	40x40x40 mm
1 PDM	Flexible Optical B.V.	-	37 channels, $\varnothing 30mm$
1 high voltage amplifier	Flexible Optical B.V.	-	40 channels, 0-300 V
2 photodiodes	TAOS, Korea	TSL250R-LF	built-in amplifier
1 computer	-	-	-
1 AD-DA system	dSpace	1 x DS1006	2.6 GHz AMD, 64-bit
		1 x DS2004	AD-card, 16-bit, 16 channels
		2 x DS2103	DA-card, 14-bit, 32 channels
1 software package	-	-	Windows XP, MATLAB
			ControlDesk
2 power supplies			-15,GND,+15V
			-5,GND,+5V

Bibliography

[1] Wikipedia, "Adaptive optics." http://en.wikipedia.org/wiki/Adaptive_optics, December 2009.

[2] O. Scot, "Adaptive optics." https://www.llnl.gov/str/Olivier.html, December 2009.

[3] L. Murray, "Smart optics: Wavefront sensor-less adaptive optics - image correction through sharpness maximisation." A thesis as part of a PhD Thesis, October 2006.

[4] M. de Boer, "Control of a thermal deformable mirror." Master Thesis, October 2003.

[5] G. Vdovin, "Optimization-based operation of micromachined deformable mirrors," *SPIE*, vol. 3353, March 1998.

[6] OKO Technologies, *Adaptive Optics Guide*. 2008.

[7] M. Zacepin, "Phd-thesis abstract: Mathematical modeling strain conditions of rock to develop mining field (russian text)." http://www.math.spbu.ru/ru/mmeh/aspdok/pub/2009/zacepin.doc, 2009.

[8] M. Y. Loktev, "Modal wavefront correctors based on nematic liquid crystals." PhD Thesis, October 2005.

[9] G. Vdovin, O. Soloviev, A. Samokhin, and M. Loktev, "Correction of low order aberrations using continuous deformable mirrors," *Optics Express 2859*, vol. 16, no. 5, March 2008.

[10] H. Song, G. Vdovin, R. Fraanje, G. Schitter, and M. Verhaegen, "Extracting hysteresis from nonlinear measurement of wavefront-sensorless adaptive optics system," *Optics Letters*, vol. 34, no. 1, January 2009.

[11] K. Furutani, M. Urushibata, and N. Mohri, "Improvement of control method for piezoelectric actuator by combining induced charge feedback with inverse transfer function compensation." Proceedings of the 1998 IEEE International Conference on Robotics and Automation, May 1998.

[12] K. Hinnen, R. Fraanje, and M. Verhaegen, "The application of initial state correction in iterative learning control and the experimental validation on a piezoelectric tube scanner." Proc. of the Institution of Mech. Eng. Part I - Journal of Systems and Control Engineering, September 2004.

[13] D. Croft, G. Shed, and S. Devasia, "Creep, hystersis, and vibration compensation for piezoactuators: Atomic force microscopy application," *Journal of Dynamics Systems, Measurement, and Control*, vol. 123, no. 35, March 2001.

[14] A. Dubra, J. S. Massa, and C. Paterson, "Preisach classical and nonlinear modeling of hysteresis in piezoceramic deformable mirrors," *Optics Express*, vol. 13, no. 22, Oktober 2005.

[15] Y. Okazaki, "A micro-positioning tool post using a piezoelectric actuator for diamond tuning machines," *Precision Engineering*, vol. 12 number =, 1990.

[16] H. Song, R. Fraanje, G. Schitter, and M. Verhaegen, "Hysteresis compensation for a piezo deformable mirror." Adaptive Optics for Industry and Medicine, July 2007.

[17] M. C. Q. Yang, C. Ftaclas and D. Toomey, "Hysteresis correction in the curvature adaptive optics system," *Journal of Optical Society of America*, vol. 22, no. 1, January 2005.

[18] K. Dirschl, J.Garn_s, L. Nielsen, J. J∅gensen, and M. S∅rensen, "Modeling the hysteresis of a scanning probe microscope," *J. Vac. Sci. Technol.B*, vol. 18, no. 2, March/April 2000.

[19] M. Booth, "Wavefront sensorless adaptive optics for large aberrations," *Optics Express*, vol. 32, no. 1, 1 January 2007.

[20] D. Debarré, M. Booth, and T. .Wilson, "Image based adaptive optics through optimisation of low spatial frequencies," *Optics Express*, vol. 15, no. 13, June 2007.

[21] E. Grisan, F. Frassetto, V. D. Deppo, G. Naletto, and A. Ruggeri, "No wavefront sensor adaptive optics system for compensation of primary aberrations by software analysis of a point source image," *Applied Optics*, vol. 46, no. 25, 1 September 2007.

[22] M. Booth, "Wavefront sensor-less adaptive optics: a model based approach using sphere packings," *Optics Express*, vol. 14, no. 4, 20 February 2006.

[23] J. Lagarias, J. Reeds, M. Wright, and P. Wright, "Convergence properties of the nelder-mead simplex method in low dimensions," *Society for Industrial and Applied Mathematics*, vol. 9, no. 1, pp. 112–147, 1998.

Glossary

List of Acronyms

AO	adaptive optics
DM	deformable mirror
PDM	piezo deformable mirror
TDM	thermal deformable mirror
CA	control algorithm
OA	optimization algorithm
VO	voltage optimization
SO	shape optimization
NM	Nelder-Mead simplex
LS	line search
QO	quadratic optimization
HC	hysteresis compensation
WFS	wavefront sensor
WFSless	wavefront-sensorless
SNR	signal to noise ratio
RMS	root mean square
PZT	lead zirconate titanate (piezoelectric material)
C-H eq.	Coleman Hodgdon equations
TUD	Technische Universiteit Delft (Delft University of Technology)
DCSC	Delft Center for Systems & Control
MATLAB	matrix laboratory

List of Symbols

$h(x, y)$	$\in \mathbb{R}$	height of wavefront in meters
$\phi_0(x, y)$	$\in \mathbb{R}$	undistorted, flat wavefront
$\phi_{dm}(x, y)$	$\in \mathbb{R}$	phase of the wavefront produced by the deformable mirror at a place (x,y) in radians
$\phi_{ab}(x, y)$	$\in \mathbb{R}$	phase of the total aberration present in the light beam at a certain place (x,y) located on the deformable mirror in radians
$\phi_{error}(x, y)$	$\in \mathbb{R}$	the error of the corrected wavefront, $\phi_{error} = \phi_{ab} + \phi_{dm}$.
Z_i		i^{th} mode of the orthogonal Zernike modes
β	$\in \mathbb{R}^m$	array of coefficients that describe the shape of the deformable mirror in orthogonal Zernike or Lukosz modes
m	$\in \mathbb{N}$	number of evaluated Zernike modes
o	$\in \mathbb{N}$	order of the Zernike mode
r	$\in \mathbb{Z}$	radial frequency of the Zernike mode
k	$\in \mathbb{N}$	number of actuators
$\mathbf{v}_k$	$\in \mathbb{R}^k$	reference voltages calculated by the controller. k is the number of actuators
$\mathbf{h}_{act}$	$\in \mathbb{R}^k$	height at the locations of the actuators, only due to the voltage applied to the piezo actuators
$\mathbf{h}_k$	$\in \mathbb{R}^k$	actual height of the deformable mirror at the locations of actuators.
$\mathbf{V}_{control}$	$\in \mathbb{R}^k$	the voltages that are calculated by the inverse hysteresis model in order to obtain a linear model between $\mathbf{v}_k$ and $\mathbf{h}_k$. k is the number of actuators
I_{photo}	$\in \mathbb{R}$	voltage produced by the photodiode measuring the light intensity behind the pinhole
$\mathbf{v}_{hyst}$	$\in \mathbb{R}$	voltage produced by the photodiode measuring the light intensity with the Foucault knife edge test
$\mathbf{v}_i$	$\in \mathbb{R}$	voltage send to the actuator which is used to extract hysteresis with help of the Foucault knife edge test